U-shaped fairings suppress vortex-induced vibrations for cylinders in cross-flow

Citation: Xie, Fangfang; Yu, Yue and Constantinides, Yiannis. "U-Shaped Fairings Suppress Vortex-Induced Vibrations for Cylinders in Cross-Flow." Journal of Fluid Mechanics 782 (October 2015): 300–332 © 2015 Cambridge University Press

As Published: http://dx.doi.org/10.1017/jfm.2015.529

Publisher: Cambridge University Press

Persistent URL: http://hdl.handle.net/1721.1/110825

Version: Original manuscript: author's manuscript prior to formal peer review

U-shaped fairings suppress vortex-induced vibrations for cylinders in cross-flow

Fangfang Xie[1], Yue Yu[2], Yiannis Constantinides[3], Michael S. Trinatafyllou[1], and George Em Karniadakis[4] †,

[1] Massachusetts Institute Technology, Cambridge, MA 02139 USA

[2]Lehigh University, Bethlehem, PA 18015 USA

[3]Chevron Energy Technology Company, 1400 Smith St., Houston, TX 77002 USA

[4]Brown University, Providence, RI USA

(Received ?; revised ?; accepted ?. - To be entered by editorial office)

We employ three-dimensional direct and large-eddy numerical simulations of the vibrations and flow past cylinders fitted with free-to-rotate U-shaped fairings placed in a cross-flow at Reynolds number $100 \leqslant Re \leqslant 10,000$. Such fairings are nearly-neutrally buoyant devices fitted along the axis of long circular risers to suppress vortex-induced vibrations (VIV). We consider three different geometric configurations, a homogeneous fairing, and two configurations (denoted A and AB) involving a gap between adjacent segments. For the latter two cases, we investigate the effect of the gap on the hydrodynamic force coefficients and the translational and rotational motions of the system. For all configurations, as the Reynolds number increases beyond 500, both the lift and drag coefficients decrease. Compared to a plain cylinder, a homogeneous fairing system (no gaps) can help reduce the drag force coefficient by 15% for reduced velocity $U^* = 4.65$, while a type A gap system can reduce the drag force coefficient by almost 50% for reduced velocity $U^* = 3.5, 4.65, 6$, and, correspondingly, the vibration response of the combined system, as well as the fairing rotation amplitude are substantially reduced. For a homogeneous fairing, the cross-flow amplitude is reduced by about 80%, whereas for fairings with a gap longer than half a cylinder diameter, VIV are completely eliminated, resulting in additional reduction in the drag coefficient. We have related such VIV suppression or elimination to the features of the wake flow structure. We find that a gap causes the generation of strong streamwise vorticity in the gap region that interferes destructively with the vorticity generated by the fairings, hence disorganizing the formation of coherent spanwise cortical patterns. We provide visualization of the incoherent wake flow that leads to total elimination of the vibration and rotation of the fairing-cylinder system. Finally, we investigate the effect of the frictional coefficient between cylinder and fairing; the effect overall is small, even when the frictional coefficients of adjacent segments are different. In some cases the equilibrium positions of the fairings are rotated by a small angle on either side of the centerline, in a symmetry-breaking bifurcation, which depends strongly on Reynolds number.

Key words: Kármán street, DNS, lock-in, VIV, flow-structure interaction, symmetry-breaking bifurcation

---

† Email address for correspondence: George_Karniadakis@brown.edu

1. Introduction

A flexibly mounted cylinder or a long flexible cylinder placed in cross-flow is subject to vibrations caused by the spontaneous initial formation of the Kármán street, a double array of vortices of alternating vorticity sign; a nonlinear feedback mechamism coupling the vibrating structure and the forming vortical patterns in the wake leads to a very rich dynamic behavior (Williamson & Govardhan 2004, 2008). The resulting vortex induced vibrations (VIV) constitute a major problem in ocean structures, in heat exchangers, and especially in the offshore industry, given the new emphasis on deep water drilling, because they can increase the drag coefficient significantly and can also cause failure by fatigue.

A great variety of passive and active flow control techniques to reduce or suppress VIV have been proposed, as reviewed in (Zdravkovich 1981; Every *et al.* 1982; Galvao *et al.* 2008). The proposed means include splitter plates (Bearman 1965; Kwon & Choi 1996; Assi *et al.* 2009; Gu *et al.* 2012; Bao & Tao 2013), (Serson *et al.* 2014), suction based flow control (Dong *et al.* 2008; Chen *et al.* 2013), moving boundary layer control (Korkischko & Meneghini 2012), slits parallel to the incoming flow (Baek & Karniadakis 2009), stream-lining of the structural geometry (Pontaza & Menon 2008; Corson *et al.* 2014), helical strakes (Allen *et al.* 2003; Trim *et al.* 2005), and other add-on devices for passive control (Owen *et al.* 2001; Bearman & Branković 2004).

Helical strakes have been an effective solution to suppress VIV in ocean engineering structures since the late 1960s. In the helical strakes model, the coherent vortex shedding along the span of the structure is disrupted by the strakes, leading to a reduction of the oscillatory lift forces along the cylinder (Allen *et al.* 2008). However, an undesirable side effect of helically straked cylinders at all Reynolds numbers, including supercritical flow conditions, is higher mean drag coefficient (Pontaza *et al.* 2007). Higher drag force exerted on the riser may cause it to flex significantly along its length, which, for example, may lead to an interrruption of drilling operations during periods of high current conditions.

Fairings can be an attractive alternative to helical strakes, because they can suppress VIV and simultaneously lower the drag force. Unlike strakes, which are fixed to the riser, fairings are nearly-neutrally buoyant devices, which are fitted along the axis of risers. However, in order for fairings to be effective, they must be free to rotate to align themselves with the flow; if rotation is impeded, then not only their effectiveness decreases substantially, but drag increases, steady side lift develops, and galoping oscillations may result. As a result, fairings require careful design and installation. A short fairing design with a chord of about 1.5D and with a thin tail but no stabilizer fins, is described in (Allen *et al.* 2008). In the same paper, the authors compared the basic performance of both helical strakes and fairing devices and found that fairings suppress VIV more efficiently than helical strakes, due to their slightly better performance when marine growth is present, and their substantially better performance for cylinders located downstream from other cylinders.

A U-shaped fairing with an open back, shown in figure 1, is a commercial design used for suppressing riser VIV. Pontaza & Menon (2008) numerically investigated the hydrodynamic performance of this fairing design and found that it experiences a low drag coefficient ($C_d = 0.52$ at $Re \approx 10^6$). The splitter plates prevent the near-wake interaction of the opposite-sign vorticity shear layers emanating from the sides of the fairing module. Therefore, flow unsteadiness in the near-wake of the riser is weakened. They also recorded small amplitude drag and lift force coefficients, which may imply that this configuration is effective. However, in Pontaza & Menon (2008) a stationary design

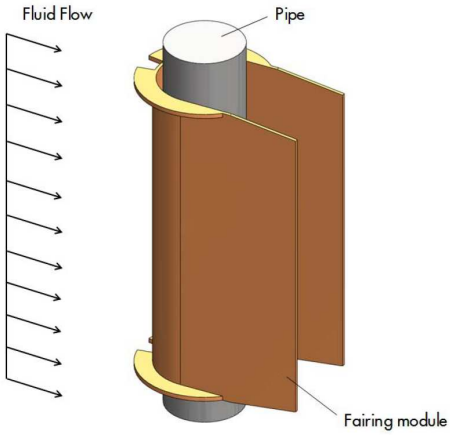

Figure 1: U-shaped fairing module on a 4.5 inch pipe from (Pontaza *et al.* 2012).

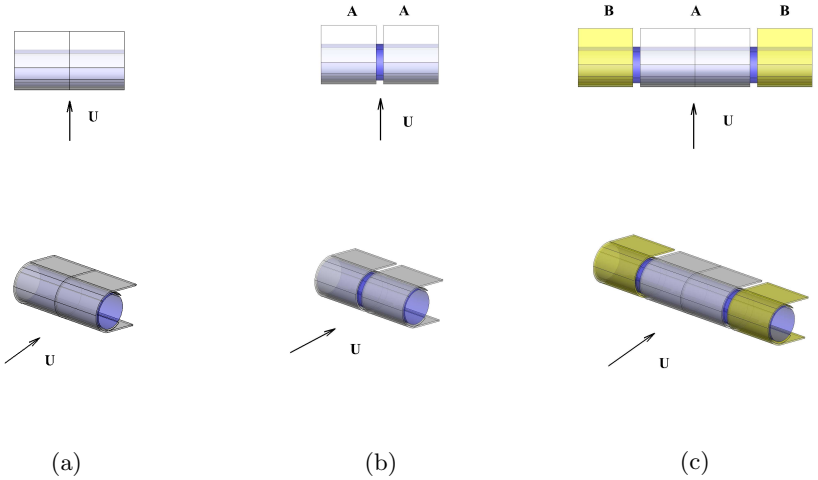

(a) (b) (c)

Figure 2: Geometry of fairing configurations considered in this work. (a) Homogeneous fairing-cylinder system. (b) Fairing-cylinder system of type A. (c) Fairing-cylinder system of type AB.

was studied, presumably due to the complexity associated with the simulation of free VIV motion of the fairing-cylinder system.

Yu *et al.* (2015) performed numerical simulations of the freely vibrating fairing-cylinder system with the spectral element solver NEKTAR (Karniadakis & Sherwin 2013), mostly in two-dimensions, hence neglecting the gaps between adjacent fairing modules. They employed a partitioned fluid-structure interaction (FSI) method (Baek & Karniadakis 2012), which led to reasonable computational scalability and efficiency. Since the rotational friction plays an important role in suppressing VIV and reducing the drag force (Assi *et al.* 2009), a free-to-rotate fairing model was adopted in their simulations. They found that VIV is, indeed, drastically reduced at low Reynolds numbers and the role of the frictional coefficient between the fairing and cylinder was explained and quantified. Due to the low

rotational inertia of the fairing, the added-mass effect (Causin *et al.* 2005) is very strong and can severely affect the flow-structure interaction. To this end, a new method of fictitious mass (Baek & Karniadakis 2012; Yu *et al.* 2013) was employed, where additional acceleration terms are introduced in the structure solver to balance the added-mass effect caused by low rotational inertia, and provide stabilization when problems with large fairing rotations arise. Yu *et al.* (2015) also performed a three-dimensional study, where fairings of finite length are placed along the cylinder span. The fairings were homogeneous, fitted along the cylinder without gaps. However, in industrial applications fairings of length 3-5 diameters are fitted along the riser and there always exists a gap between adjacent fairing modules.

In the present study, we will extend the previous work by (Yu *et al.* 2015) to higher Reynolds numbers and, in particular, we will investigate the effect of the gap between adjacent fairings. Three different three-dimensional geometric models for the fairing-cylinder system are adopted, as shown in figure 2. In all configurations, periodic boundary conditions are imposed on both ends of the model in the spanwise direction, hence simulating very long fairing-cylinder systems. First, a homogeneous fairing-cylinder system is considered, which is an extension of the two-dimensional geometry along the spanwise direction. The second is a type A system with a gap (denoted by G in the paper) following the actual fairing module used in Chevron's experiment setup. The third is a fairing-cylinder system of type AB with gaps between adjacent fairings. For the type A system, the gray part represents the fairing, while the blue part represents the cylinder. For the type AB configuration, the yellow part represents the second adjacent fairing. As we will show, a gap between adjacent fairings can dramatically alter the wake pattern, leading to significant drag reduction and VIV suppression and possibly to total VIV elimination. This is linked to a fundamental change in the vorticity production and redistribution around the fairing-cylinder system that we investigate in the current work.

The paper is organized as follows. In section 2, the physical model and numerical method are presented. Then, the equations of motion for the fairing-cylinder systems of type A and type AB are presented in section 3. Simulation results for the free motion of homogeneous fairing-cylinder system at high Reynolds number are presented in section 4. Comparison of two-dimensional and three-dimensional simulation results of homogeneous fairing-cylinder system for various friction coefficients at $Re = 1,000$ are shown in section 4.1. We also provide numerical results of vibrating fairings at $Re = 10,000$ in section 4.2. Since a gap between fairings along the cylinder span affects the drag force and VIV motions, we conduct systematic numerical simulations and present the corresponding results in section 5. First, the flow around the periodic type A system at different gap distances is simulated at $Re = 100$ in section 5.1. Then, the vibration behavior of fairings with gap $G = 0.5D$ is investigated at three different Re ($Re = 100$, $Re = 500$ and $Re = 1,000$) in section 5.2. Finally, the VIV of type AB systems are studied at $Re = 100$ and $Re = 500$ in section 5.3. We summarize the main points of our paper in section 6.

2. Problem definition and simulation set up

In a previous study (Yu *et al.* 2015), direct numerical simulations were mostly focused on two-dimensional and low Re ($100 \leqslant Re \leqslant 1,000$) flow for a two-dimensional fairing-cylinder system, as shown in figure 3. The cylinder is free to respond in both the cross-flow and streamwise directions. The fairing moves following the cylinder, but with an additional degree of freedom because it can rotate around the cylinder axis, subjected to hydrodynamic torque. Due to the gap and the three-dimensionality of the geometry, the equations for the fairing and cylinder motions are different and are presented in section

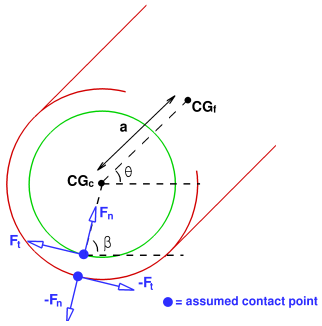

Figure 3: Coordinate system and symbol definition for the fairing and cylinder motions. Here we use green to represent the cylinder and red to represent the fairing, while the contact forces are marked by blue.

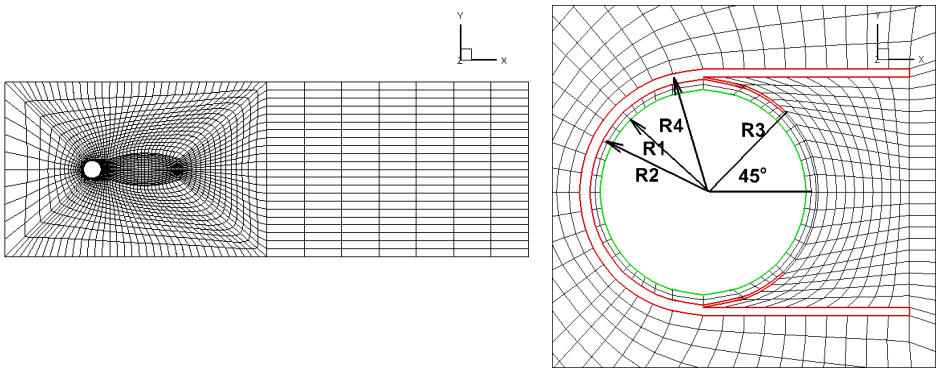

(a) (b)

Figure 4: Fluid mesh around the fairing-cylinder system. (a) Spectral element mesh for the fluid solver. Domain size: $[-5, 20] \times [-5, 5] \times [0, L_c]$, where L_c is the length of the cylinder along its axis. The origin $(0, 0, 0)$ is located at the center of cylinder and the diameter of cylinder is $D_c = 1$. (b) Details of mesh near the fairing-cylinder system; here we use green to represent the cylinder and red to represent the fairing.

3. In the fairing-cylinder system of type A, the effect of gap is introduced by the length ratio L_f/L_c, where L_f is spanwise length of fairing, and L_c is spanwise length of cylinder; here, we have $L_c = L_f + G$. Hence, if there is no gap between fairings, with $G = 0$, we obtain the structure equations for a homogeneous fairing-cylinder system. In the fairing-cylinder system of type AB, there are eight equations of motion. The relationship between cylinder length and fairing length is $L_c = L_f + L_g + 2G$, where L_g is the spanwise length of the second fairing.

For the fluid part, the flow is simulated in several 3D domains: a small domain $[-5, 20] \times [-5, 5] \times [0, L_c]$ with the origin $(0, 0, 0)$ located at the center of cylinder for $Re \leqslant 1,000$; for higher Reynolds number a bigger and finer mesh is employed as discussed in section 4.2. The effect of blockage as well as the sensitivity to the spectral element polynomial order have been quantified in figures 5, 10 and 15 of Yu *et al.* (2015); it was also re-examined in the current 3D simulations. A solid cylinder with diameter $D_c = 1$ is placed at the origin with a fairing surrounding it. For the fluid solver we used a mesh consisting

Parameter	Value
Cylinder diameter D_c	1.0
Fairing (circular part) diameter D_f	1.2
Length in spanwise direction L_f	3
Gap distance between fairings G	$0.2 - 1.5$
Free-stream velocity U	1.0
Cylinder natural frequency f_N	0.215
Reduced velocity $U^* = U/f_N D_c$	4.65
Cylinder mass m_c	6.0
Fairing mass m_f	1.0
Cylinder spring constant $k_x, k_y = 4\pi^2 m_c f_N^2$	10.949
Fairing rotational inertia I_f	0.6
Cylinder-fairing gravity center distance a	0.0851
Fluid density ρ_f	1.0

Table 1: Non-dimensional parameters used in the numerical simulations based on the cylinder diameter D_c, free-stream velocity U and fairing mass m_f.

of hexahedral elements, built by extrusion of a 2D mesh shown in figure 4. The boundary conditions are as follows: at the inlet, a uniform steady flow with $U = 1$ is imposed, while at the outlet we employ a zero Neumann boundary condition. Along the cross-flow and spanwise directions, a periodic boundary condition is applied. The fairing is composed of two parts: (1) the circular body part, which covers $\frac{3}{4}$ of the cylinder and is centered at the cylinder center with radius 0.6; (2) a pair of parallel plates attached to the top and bottom points of the circular part of the fairing (see the red part in figure 3). Unlike the configuration used in two-dimensional simulations, the thickness of the plates in the fairing geometry is nonzero here. Figure 4(b) provides the detailed configuration of the fairing. The parameters in the plot are $R_2 = 0.55, R_3 = 0.56, R_4 = 0.6$. In the undisturbed configuration the plates are parallel to the streamwise direction, with a length of 1.0, i.e., equal to one cylinder diameter D. The fairing's center of gravity is located at $(0.085, 0)$ in the (x, y) plane.

A fictitious inertia method is employed to stabilize the fluid-structure interaction simulations for fairings with low inertia in order to solve the coupled Navier-Stokes and structural equations (Baek & Karniadakis 2012). For the fluid model, we employ the incompressible Navier-Stokes equation expressed in an arbitrary Lagrangian-Eulerian framework (Hughes *et al.* 1981). For the solid model, we discretize the structure system in time using the Newmark scheme, and apply an additional inertial term following the fictitious inertia method. Specifically, unlike in the simulations of Baek & Karniadakis (2011), here we only needed to stabilize the rotational motion, and not the translational motion; hence, we employed only a fictitious inertia term. According to numerical tests conducted in Yu *et al.* (2015), an effective fictitious inertia coefficient f_I takes values around 2.0 and is only weakly dependent on the Re. Here we employ spectral elements of order $p = 3$ and $p = 5$ in all simulations. Simulations were performed using the physical and numerical parameters in table 1, unless stated otherwise.

All parameters are non-dimensionalized based on the cylinder diameter D_c, free-stream velocity U, and fairing mass m_f. The mass ratio between cylinder and fairing is $m_c/m_f = 6$, matching the value used in experiments conducted by Chevron. Moreover, for this mass ratio, the largest amplitude of oscillation is found around $U^* = 4.65$ for the homogeneous

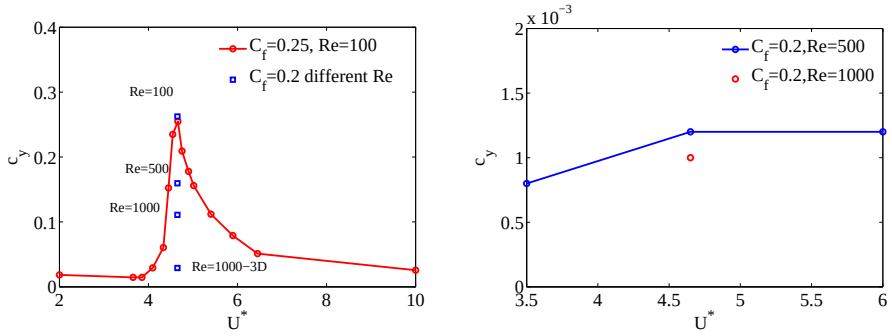

(a) (b)

Figure 5: VIV response c_y for (a): the homogeneous fairing-cylinder system, and (b): the type A system, as a function of reduced velocity U^*.

fairing system at $Re = 100$. The response at the same U^* value decreases for higher Re – see figure 5(a). For the type A system, in addition to $U^* = 4.65$, we also investigated the response at reduced velocities 3.5 and 6 at $Re = 500$. From Fig. 5(b), it is seen that the VIV response is virtually eliminated for all values of U^*. This is the reason we focus our simulations on $U^* = 4.65$.

3. Cylinder and fairing models: Governing equations

3.1. *Fairing-cylinder system of type A*

First, we introduce the structure equations for the 3D fairing-cylinder system of type A. The cylinder is subjected to VIV with two degrees of freedom (DOF) in the (x, y) plane. In each (x, y) section, the fairing and the cylinder are concentric while the fairing is in contact with the cylinder and is free to rotate. There is a small gap between the fairing and cylinder with a single point of contact, where the fairing is pressed against the cylinder; the contact angle β denotes the position of the contact point. As shown in figure 3, for each (x, y) section the system allows body motions with five DOF, including the cylinder's horizontal and vertical motions (c_x and c_y), and the fairing's horizontal, vertical motions (f_x and f_y) and rotational angle (θ). Here we define some symbols to be used in the equations of motion, see table 2. To derive the equations of motion for the fairing-cylinder system of type A, we make the following assumptions:

(a) There is no damping force acting on the structure in the translational and rotational directions;

(b) The cylinder and the fairing are always in contact at a single point in the (x, y) plane ;

(c) The tangential contact force F_t between the cylinder and the fairing in the (x, y) plane is uniform. It is related to the normal contact force F_n following $F_t = f_c F_n$, where f_c is proportional to the sign function of $\dfrac{\partial\theta}{\partial t}$, with a constant sliding friction coefficient C_f, i.e.,

$$f_c = C_f \mathrm{sgn}\left(\frac{d\theta}{dt}\right). \tag{3.1}$$

Here C_f can be seen as a measure of the rotational damping and frictional force. More details are provided in the appendix of (Yu *et al.* 2015).

Symbols	Expression
CG_c, CG_f	Center of gravity of cylinder and fairing, respectively
a	Distance from CG_c to CG_f
f_c	Coefficient of friction between the cylinder and fairing
C_f	Non-dimensional coefficient for the rotational damping and frictional force
F_{chx}, F_{chy}	Hydrodynamic force applied on the cylinder in the x and y direction, respectively
k_x, k_y	Cylinder spring constant in the x and y directions, respectively
F_{fhx}, F_{fhy}	Hydrodynamic force applied on the fairing in the x and y directions, respectively
I_f	Fairing rotational inertia about CG_f
m_c, m_f	Mass of cylinder and fairing, respectively
M_{fh}	Hydrodynamic angular momentum applied on the fairing about CG_f
R	Cylinder radius
β	Contact angle
F_n	Cylinder-fairing normal contact force
F_t	Cylinder-fairing tangential contact force
L_f	Total spanwise length of fairing in the type A system
L_c	Spanwise length of cylinder in the type A system ($L_c = L_f + G$)

Table 2: Symbols used in the type A system, see geometries in figure 2(a)(b).

Based on these assumptions, the equations of motion for the *cylinder* are written about CG_c:

$$\begin{aligned} m_c \frac{\partial^2 c_x}{\partial t^2} L_c + k_x c_x L_c - F_n(\cos\beta + f_c \sin\beta) L_f = F_{chx}, \\ m_c \frac{\partial^2 c_y}{\partial t^2} L_c + k_y c_y L_c - F_n(\sin\beta - f_c \cos\beta) L_f = F_{chy}, \end{aligned} \tag{3.2}$$

and the equations of motion for the *fairing* are written about CG_f:

$$\begin{aligned} m_f \frac{\partial^2 f_x}{\partial t^2} L_f + F_n(\cos\beta + f_c \sin\beta) L_f = F_{fhx}, \\ m_f \frac{\partial^2 f_y}{\partial t^2} L_f + F_n(\sin\beta - f_c \cos\beta) L_f = F_{fhy}. \end{aligned} \tag{3.3}$$

From figure 3, we can see that the centers of gravity of the cylinder and fairing are geometrically related as:

$$c_x = f_x - a\cos\theta, \;\; c_y = f_y - a\sin\theta. \tag{3.4}$$

Substituting these expressions into (3.2), the equations of motion for the *cylinder* become:

$$\begin{aligned} & m_c \left[\frac{\partial^2 f_x}{\partial t^2} + a \left(\left(\frac{\partial \theta}{\partial t} \right)^2 \cos\theta + \frac{\partial^2 \theta}{\partial t^2} \sin\theta \right) \right] L_c \\ & + k_x \left[f_x - a\cos\theta \right] L_c - F_n \left(\cos\beta + f_c \sin\beta \right) L_f = F_{chx}, \end{aligned} \tag{3.5a}$$

$$\begin{aligned} & m_c \left[\frac{\partial^2 f_y}{\partial t^2} + a \left(\left(\frac{\partial \theta}{\partial t} \right)^2 \sin\theta - \frac{\partial^2 \theta}{\partial t^2} \cos\theta \right) \right] L_c \\ & + k_y \left[f_y - a\sin\theta \right] L_c - F_n \left(\sin\beta - f_c \cos\beta \right) L_f = F_{chy}. \end{aligned} \tag{3.5b}$$

In addition, we can derive an equation for the angular momentum. The total angular momentum $I_f\ddot{\theta}$ about CG_f should be equal to the resultant angular momentum exerted by the fairing-cylinder contact force and the hydrodynamic angular momentum M_{fh} from the fluid. Specifically, the torque of the fairing-cylinder normal contact force F_n about CG_f is $a\sin(\beta-\theta)$, and the torque of the fairing-cylinder tangential contact force F_t is $-(a\cos(\beta-\theta)+R)$. Therefore, we have the resultant angular momentum as

$$M_{fh} + F_n a\sin(\beta-\theta)L_f - F_t(a\cos(\beta-\theta)+R)L_f.$$

By substituting the relation $F_t = f_c F_n$, the conservation of angular momentum can be expressed as:

$$I_f\frac{\partial^2\theta}{\partial t^2}L_f - F_n[a\sin(\beta-\theta) - af_c\cos(\beta-\theta) - Rf_c]L_f = M_{fh}. \tag{3.6}$$

Combining the equations of motion for the fairing (3.3) and the equations for the cylinder (3.5), we obtain a system with 5 equations consisting of 5 unknowns $(f_x, f_y, \theta, \beta, F_n)$:

$$\begin{aligned} &m_c\left[\frac{\partial^2 f_x}{\partial t^2} + a\left(\left(\frac{\partial\theta}{\partial t}\right)^2\cos\theta + \frac{\partial^2\theta}{\partial t^2}\sin\theta\right)\right]L_c \\ &+ k_x\left[f_x - a\cos\theta\right]L_c - F_n\left(\cos\beta + f_c\sin\beta\right)L_f = F_{chx}, \end{aligned} \tag{3.7a}$$

$$\begin{aligned} &m_c\left[\frac{\partial^2 f_y}{\partial t^2} + a\left(\left(\frac{\partial\theta}{\partial t}\right)^2\sin\theta - \frac{\partial^2\theta}{\partial t^2}\cos\theta\right)\right]L_c \\ &+ k_y\left[f_y - a\sin\theta\right]L_c - F_n\left(\sin\beta - f_c\cos\beta\right)L_f = F_{chy}. \end{aligned} \tag{3.7b}$$

$$m_f\frac{\partial^2 f_x}{\partial t^2}L_f + F_n(\cos\beta + f_c\sin\beta)L_f = F_{fhx}, \tag{3.7c}$$

$$m_f\frac{\partial^2 f_y}{\partial t^2}L_f + F_n(\sin\beta - f_c\cos\beta)L_f = F_{fhy} \tag{3.7d}$$

$$I_f\frac{\partial^2\theta}{\partial t^2}L_f - F_n[a\sin(\beta-\theta) - af_c\cos(\beta-\theta) - R_cf_c]L_f = M_{fh}. \tag{3.7e}$$

3.2. *Fairing-cylinder system of type AB*

In the type AB system, there are two different fairings interacting with the cylinder within the computational domain. Just as in the type A system, the setup of the second fairing is the same as the first fairing, except that it is located between two other fairings at the ends (which due to periodicity are effectively part of the same fairing). The type AB system allows motions with eight DOF, including the cylinder's horizontal and vertical motions (c_x and c_y), the first fairing's horizontal, vertical motions (f_x and f_y) and rotational angle (θ), and the second fairing's horizontal, vertical motions (g_x and g_y) and rotational angle (ζ). Here we define the symbols to be used in the equations of motion for the fairings in table 3. To derive the equations of motions for the fairing-cylinder system of type AB, we employ additional assumptions:

(a) The cylinder and the two fairings are always in contact at a single point in the (x, y) plane for each fairing;

(b) The tangential contact force G_t between the cylinder and the second fairing in the (x, y) plane is uniform. It is related to the normal contact force G_n following $G_t = f_g G_n$, where f_g is proportional to the sign function of $\dfrac{\partial\zeta}{\partial t}$ with a constant sliding friction

Symbols	Expression
CG_g	Center of gravity of second fairing
f_g	Coefficient of friction between the cylinder and second fairing.
F_{ghx}, F_{ghy}	Hydrodynamic force applied on the second fairing in the x and y directions
I_g	Fairing rotational inertia about CG_g
m_g	Mass of second fairing
M_{gh}	Hydrodynamic angular momentum applied on the second fairing about CG_g
α	Contact angle between cylinder and second fairing
G_n	Cylinder-fairing normal contact force
G_t	Cylinder-fairing tangential contact force
L_g	Entire spanwise length of second fairing in fairing-cylinder system of type AB
L_c	Spanwise length of cylinder in fairing-cylinder system of type AB ($L_c = L_f + L_g + 2G$)

Table 3: Symbols used in the type AB system – see geometry in figure 2(c).

coefficient C_g, i.e.,

$$f_g = C_g \mathrm{sgn}\left(\frac{d\zeta}{dt}\right). \tag{3.8}$$

Here C_g represents a measure of the rotational damping and frictional force for the second fairing.

Based on these assumptions, the equations of motion for the *cylinder* are written about the CG_c as:

$$\begin{aligned} m_c\frac{\partial^2 c_x}{\partial t^2}L_c + k_x c_x L_c - F_n(\cos\beta + f_c\sin\beta)L_f - G_n(\cos\alpha + f_g\sin\alpha)L_g = F_{chx},\\ m_c\frac{\partial^2 c_y}{\partial t^2}L_c + k_y c_y L_c - F_n(\sin\beta - f_c\cos\beta)L_f - G_n(\sin\alpha - f_g\cos\alpha)L_g = F_{chy}, \end{aligned} \tag{3.9}$$

and the equations of motion for the *first fairing* are written about the CG_f, which is the same as in equation (3.3). Also, the equations of motion for the *second fairing* are written about CG_g, which is similar to equation (3.3):

$$\begin{aligned} m_g\frac{\partial^2 g_x}{\partial t^2}L_g + G_n(\cos\beta + f_g\sin\beta)L_g = F_{ghx},\\ m_g\frac{\partial^2 g_y}{\partial t^2}L_g + G_n(\sin\beta - f_g\cos\beta)L_g = F_{ghy}. \end{aligned} \tag{3.10}$$

Since there are two different fairings rotating and interacting around the cylinder, we can see that the centers of gravity of the cylinder and the two fairings are geometrically related as:

$$\begin{aligned} f_x = c_x + a\cos\theta,\ \ f_y = c_y + a\sin\theta.\\ g_x = c_x + a\cos\zeta,\ \ g_y = c_y + a\sin\zeta. \end{aligned} \tag{3.11}$$

Substituting these expressions into (3.10) and (3.3), the equations of motion for fairing-cylinder system of type AB become:

$$
\begin{aligned}
&m_f\left[\frac{\partial^2 c_x}{\partial t^2}-a\left(\left(\frac{\partial\theta}{\partial t}\right)^2\sin\theta+\frac{\partial^2\theta}{\partial t^2}\cos\theta\right)\right]L_f+F_n\left(\cos\beta+f_c\sin\beta\right)L_f=F_{fhx},\\
&m_f\left[\frac{\partial^2 c_y}{\partial t^2}+a\left(\left(\frac{\partial\theta}{\partial t}\right)^2\cos\theta-\frac{\partial^2\theta}{\partial t^2}\sin\theta\right)\right]L_f+F_n\left(\sin\beta-f_c\cos\beta\right)L_f=F_{fhy}.\\
&m_g\left[\frac{\partial^2 c_x}{\partial t^2}-a\left(\left(\frac{\partial\zeta}{\partial t}\right)^2\sin\zeta+\frac{\partial^2\zeta}{\partial t^2}\cos\zeta\right)\right]L_g+G_n\left(\cos\alpha+f_g\sin\alpha\right)L_g=F_{ghx},\\
&m_g\left[\frac{\partial^2 c_y}{\partial t^2}+a\left(\left(\frac{\partial\zeta}{\partial t}\right)^2\cos\zeta-\frac{\partial^2\zeta}{\partial t^2}\sin\zeta\right)\right]L_g+G_n\left(\sin\alpha-f_g\cos\alpha\right)L_g=F_{ghy}.
\end{aligned}
\tag{3.12}
$$

In addition, we can derive another equation from the conservation of angular momentum for the second fairing, which is the same as the fist fairing in equation 3.6.

$$
I_g\frac{\partial^2\zeta}{\partial t^2}L_g-G_n[a\sin(\alpha-\zeta)-af_g\cos(\alpha-\zeta)-R_cf_g]L_g=M_{gh}. \tag{3.13}
$$

With the type AB system, we can obtain a system with 8 equations consisting of 8 unknowns,$(c_x, c_y, \theta, \beta, F_n, \zeta, \alpha, G_n)$:.

$$
\begin{aligned}
&m_c\frac{\partial^2 c_x}{\partial t^2}L_c+k_xc_xL_c-F_n(\cos\beta+f_c\sin\beta)L_f-G_n(\cos\alpha+f_g\sin\alpha)L_g=F_{chx},\\
&m_c\frac{\partial^2 c_y}{\partial t^2}L_c+k_yc_yL_c-F_n(\sin\beta-f_c\cos\beta)L_f-G_n(\sin\alpha-f_g\cos\alpha)L_g=F_{chy},\\
&m_f\left[\frac{\partial^2 c_x}{\partial t^2}-a\left(\left(\frac{\partial\theta}{\partial t}\right)^2\sin\theta+\frac{\partial^2\theta}{\partial t^2}\cos\theta\right)\right]L_f+F_n\left(\cos\beta+f_c\sin\beta\right)L_f=F_{fhx},\\
&m_f\left[\frac{\partial^2 c_y}{\partial t^2}+a\left(\left(\frac{\partial\theta}{\partial t}\right)^2\cos\theta-\frac{\partial^2\theta}{\partial t^2}\sin\theta\right)\right]L_f+F_n\left(\sin\beta-f_c\cos\beta\right)L_f=F_{fhy}.\\
&m_g\left[\frac{\partial^2 c_x}{\partial t^2}-a\left(\left(\frac{\partial\zeta}{\partial t}\right)^2\sin\zeta+\frac{\partial^2\zeta}{\partial t^2}\cos\zeta\right)\right]L_g+G_n\left(\cos\alpha+f_g\sin\alpha\right)L_g=F_{ghx},\\
&m_f\left[\frac{\partial^2 c_y}{\partial t^2}+a\left(\left(\frac{\partial\zeta}{\partial t}\right)^2\cos\zeta-\frac{\partial^2\zeta}{\partial t^2}\sin\zeta\right)\right]L_g+G_n\left(\sin\alpha-f_g\cos\alpha\right)L_g=F_{ghy}.\\
&I_f\frac{\partial^2\theta}{\partial t^2}L_f-F_n[a\sin(\beta-\theta)-af_c\cos(\beta-\theta)-Rf_c]L_f=M_{fh}\\
&I_g\frac{\partial^2\zeta}{\partial t^2}L_g-G_n[a\sin(\alpha-\zeta)-af_g\cos(\alpha-\zeta)-Rf_g]L_g=M_{gh}.
\end{aligned}
\tag{3.14}
$$

4. VIV of homogeneous fairing system

By conducting simulations with varying initial perturbations, we found that the flow around the fairing is three-dimensional at $Re = 1,000$. To perform three-dimensional simulations, we extrude the fairing model in two-dimensions along the spanwise direction by a length $L = 3D$, where D is the cylinder diameter. Typically, in applications the spanwise length of the U-shape fairing configuration is in the range of $3D-5D$ (Pontaza &

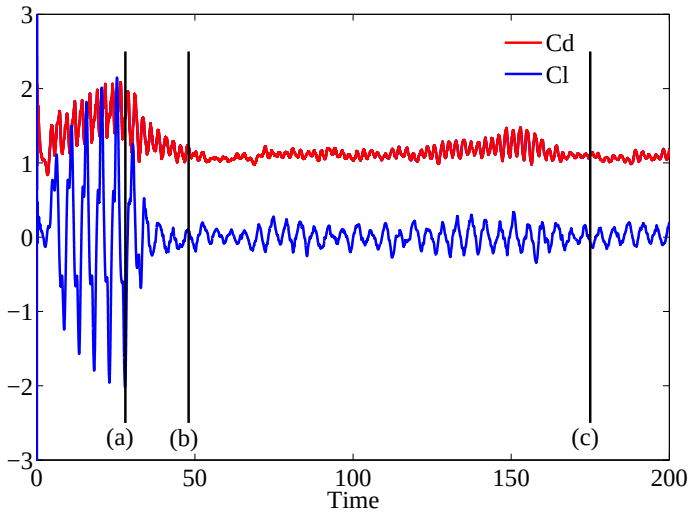

Figure 6: Transition to three-dimensionality (static configuration): time traces of hydrodynamic drag and lift coefficients on the fairing part for homogeneous fairing system at $Re = 1,000$.

Menon 2008). Here we use the value at the lower end of the range to reduce computational cost. We consider first the flow transition to three-dimensionality and its effects on the vibration of fairing (see section 4.1) at $Re = 1,000$. We also perform large-eddy simulations (LES) at a higher Reynolds number, $Re = 10,000$ in section 4.2. To this end, we will employ a new LES model we implemented recently in NEKTAR based on the variational multi scale large-eddy simulation (VMLES) model (Luo *et al.* 2011).

We define the drag and lift coefficients as:

$$C_d = \frac{F_d}{0.5\rho U^2 DL} \tag{4.1a}$$

$$C_l = \frac{F_l}{0.5\rho U^2 DL}, \tag{4.1b}$$

where F_d and F_l are the drag and lift forces, respectively. These are denoted separately, as F_{chx} and F_{chy} for the cylinder, and F_{fhx} and F_{fhy} for the fairing. For the fairing, the diameter is $D_f = 1.2$ and the spanwise length is $L_f = 3D$ for all simulations. For the cylinder, the diameter is $D_c = 1$ and the spanwise length depends on the gap G, which is $L_c = L_f + G$ for the homogeneous fairing-cylinder system and for the fairing-cylinder system of type A; and $Lc = L_f + L_g + 2G$ for the fairing-cylinder system of type AB.

4.1. *Effect of three-dimensionality*

First, we simulated the 3D flow around a stationary fairing to obtain initial conditions for the flow field for the moving fairing simulations. Figure 6 shows the time traces of the drag and lift coefficients of the fairing, which have been used in Yu *et al.* (2015). After time $t \geqslant 34$, both the drag and lift coefficients drop quickly and exhibit a non-periodic behavior, marking the transition from 2D flow to 3D flow. The fairing experiences a significantly lower drag and lift force in 3D flow compared to 2D flow. Instantaneous vorticity contours in cross-flow direction (ω_y) are used to represent the transition from two- to three-dimensionality. We present three different snapshots of ω_y contours (a) $t =$

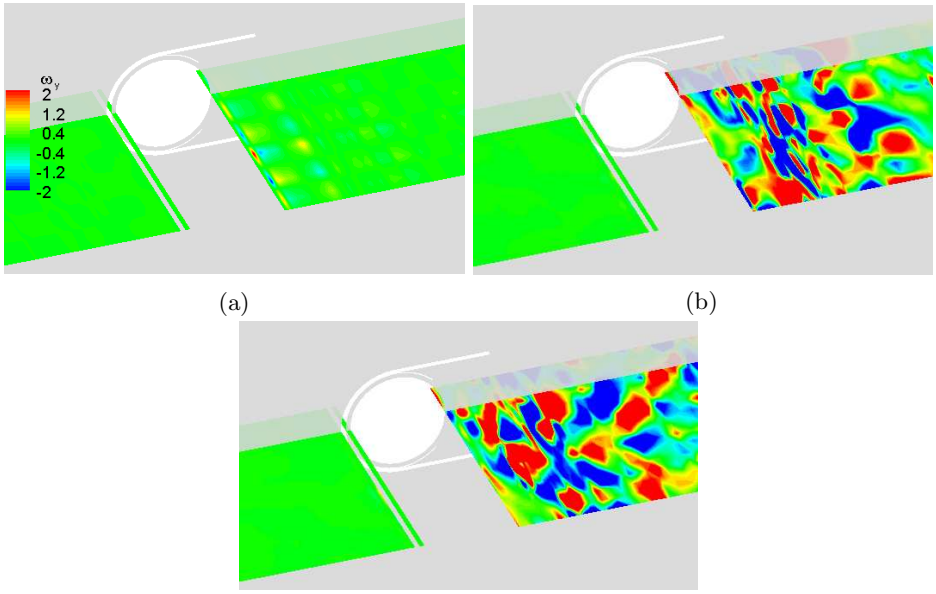

Figure 7: Instantaneous vorticity contours in the cross-flow direction (ω_y) around the homogeneous fairing at the centerline plane ($x \in (-1.7, 5.5), y = 0, z \in (0, 3)$) at $Re = 1,000$. (a): t= 28 (b): t= 48 (c): t= 175.

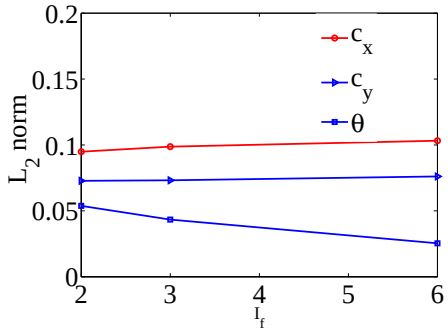

Figure 8: L_2 norm of the vibratory responses of the homogeneous fairing system (c_x, c_y, θ) versus the rotational inertia of the homogeneous fairing, I_f, for constant friction coefficient $C_f = 0.2$ at $Re = 1,000$.

$28s$, (b) $t = 48s$, (c) $t = 175s$ corresponding to flow at a 2D state, transition state, and 3D fully developed state in figure 7. The intensity of three-dimensionality is already high in the transition state as shown in figure 7.

Next, we present the results for both 2D and 3D flow around moving fairings for different values of the friction coefficient C_f, ranging from 0.1 to 0.5, and compare the effect of three-dimensionality on the structural motion. The inertia of fairing is set at $I_f = 0.6$ for 3D flow, but for 2D flow a larger value is employed, $I_f = 6.0$, to prevent very large rotations and hence extreme deformation of the mesh. Figure 8 shows the effect of inertia on the structural motion for a frictional coefficient $C_f = 0.2$ and for

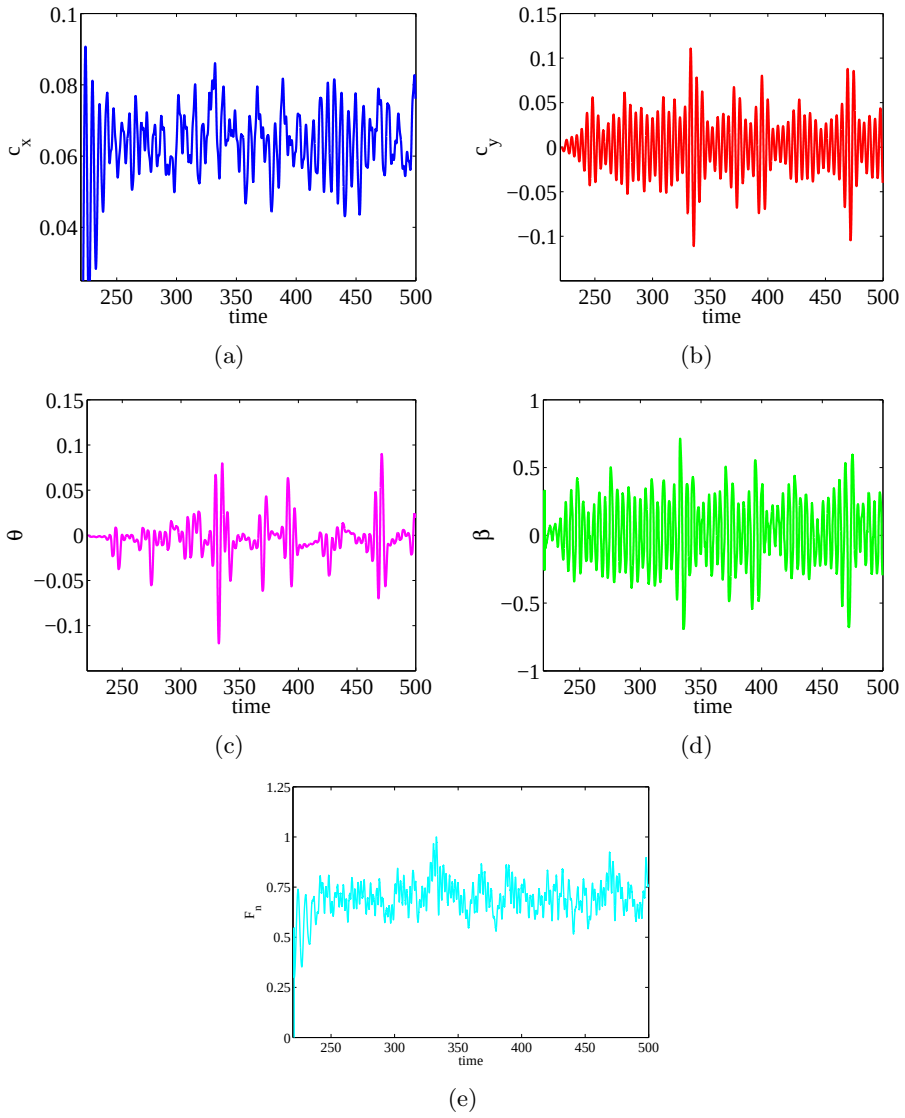

Figure 9: Time history of the motion of the homogeneous fairing system for 3D flow at $Re = 1,000$ for $C_f = 0.1$. (a) x-displacement of the cylinder c_x, (b) y-displacement of the cylinder c_y, (c) Fairing rotation angle θ, (d) Contact angle β between the fairing and the cylinder at the contact point, (e) Contact force F_n between the fairing and the cylinder at the contact point.

2D flow. Here, L_2 norm is defined as: $\sqrt{\sum_{k=1}^{n} |x_k|^2}$, where x_k denotes the time instant of the structure motion. Even though the rotation of the fairing decreases for larger I_f, the translational motion remains nearly constant. We compare the results from these two simulations to investigate the effect of three-dimensionality: In three dimensional flow, the response of the fairing follows a non-periodic motion as seen in figure 9. We use the L_2 norm in figure 10 to plot the vibration response results $(c_x, c_y, \theta, \beta)$ for 2D

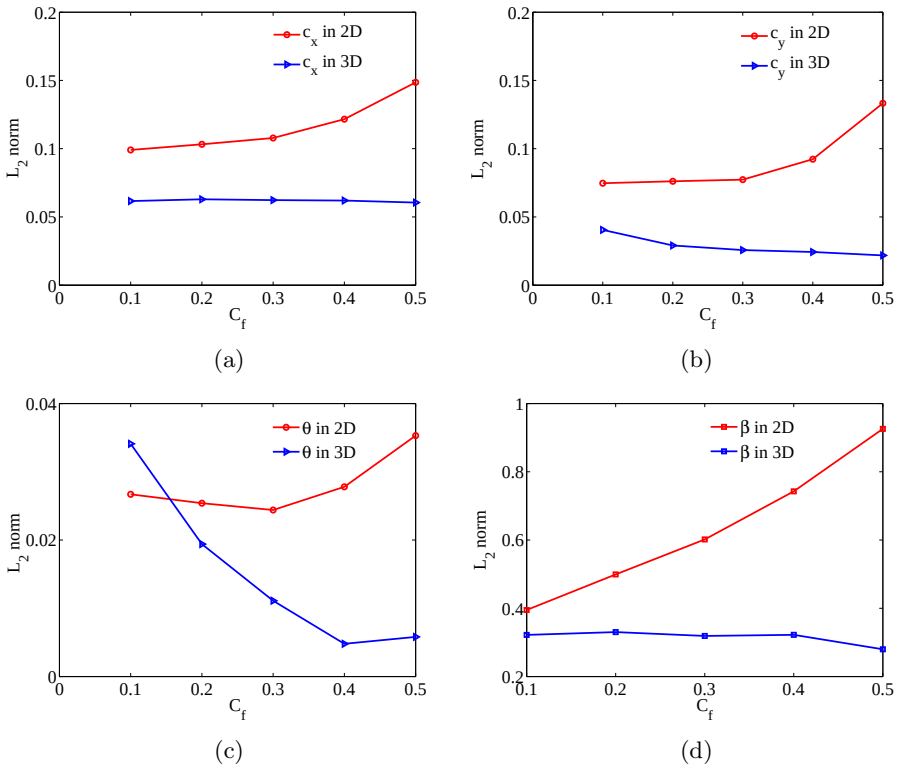

Figure 10: L_2 norm of the vibratory responses of the homogeneous fairing system at $Re = 1,000$ as function of C_f. (a) Streamwise displacement of the cylinder c_x. (b) Cross-flow displacement of the cylinder c_y. (c) Fairing rotation angle θ, (d) Contact angle β.

flow (circles) and 3D flow (triangles) at $Re = 1,000$. The 2D simulations over-predict the VIV of the structure, which is also affected by the specific value of C_f. With the increase of frictional coefficient C_f, the x-displacement of the cylinder increases in the 2D simulations; the same behavior is also observed for the cross-flow displacement, as well as the rotation angle of the fairing (θ) and the contact angle β.

To achieve the maximum VIV suppression, a frictional coefficient $C_f = 0.1$ should be selected, according to the 2D simulations. However, in 3D flow, the x-displacement of the cylinder increases to $c_x = 0.063$ at $C_f = 0.2$ and then decreases to $c_x = 0.061$ at $C_f = 0.5$. For the cross-flow displacement of the cylinder (c_y) as well as the rotation angle of the of fairing (θ), a similar pattern is observed. On the other hand, 3D simulation results at $Re = 1,000$ are more consistent with the trends of the 2D simulation results obtained at lower values of Reynolds number, i.e. at $Re = 100,\ 500$. $C_f = 0.5$ is the best choice in 3D flow at $Re = 1,000$ for the most effective VIV suppression.

4.2. *Free motion at higher Reynolds number:* $Re = 10,000$

We now conduct a 3D simulation at higher $Re = 10,000$, using a large computational domain, with the wake region extending $50D_c$, where D_c is the cylinder diameter. The free motion traces of the homogeneous fairing system at two different values of the friction coefficient C_f are compared. Figure 11 shows the time traces of structural motions, which are (a): streamwise cylinder displacement c_x, (b): cross-flow cylinder displacement

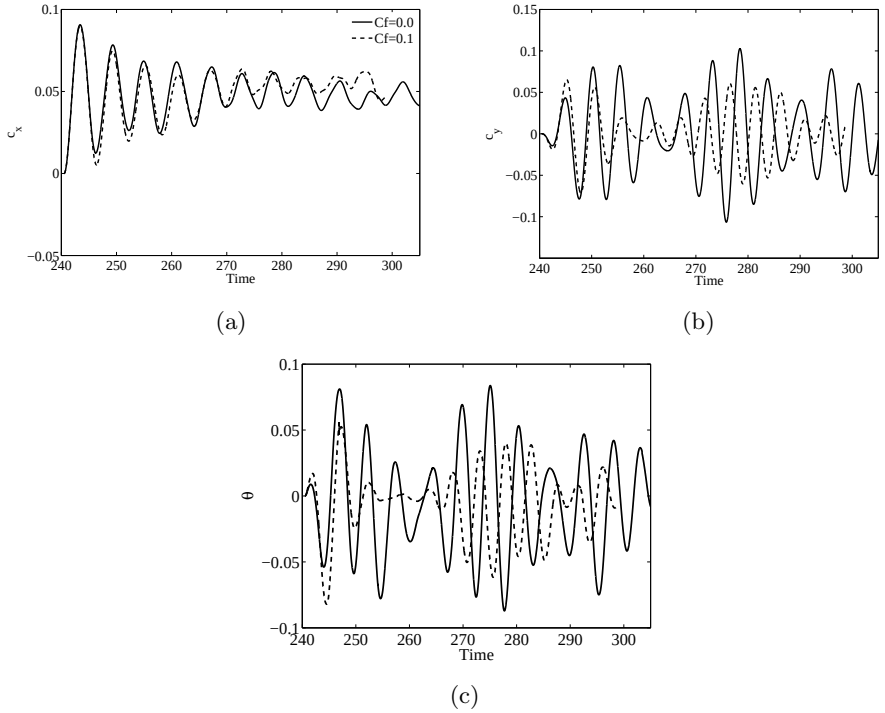

Figure 11: Time history of the motion of the homogeneous fairing system for two frictional coefficients: $C_f = 0.0$ (solid lines) and $C_f = 0.1$ (dashed lines) at Reynolds number $Re = 10,000$. (a) Streamwise cylinder displacement c_x. (b) Cross-flow cylinder displacement c_y. (c) Rotation angle θ of the fairing around the cylinder.

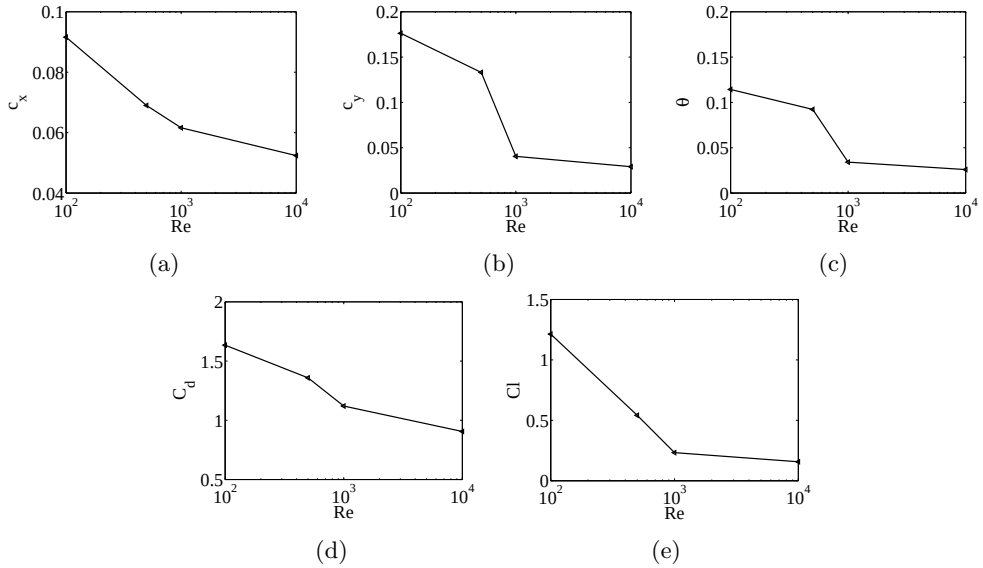

Figure 12: L_2 norm of the response and the forces $(c_x, c_y, \theta, C_d, C_l)$ for the homogeneous fairing system, with frictional coefficient $C_f = 0.1$, and for various Reynolds numbers.

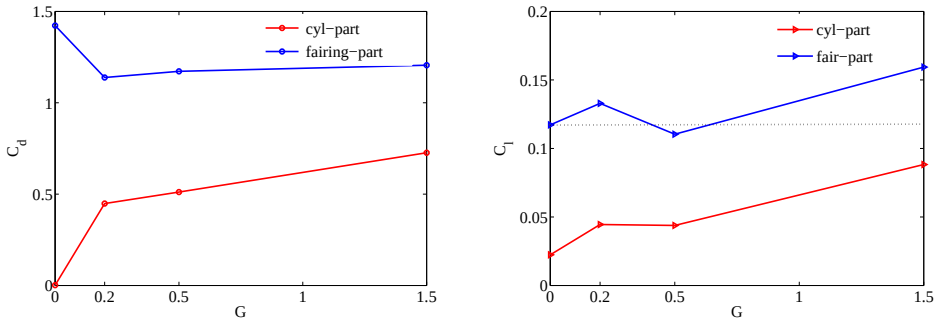

(a) (b)

Figure 13: L_2 norm of the force coefficients on the fairing and the cylinder of a stationary type A system at $Re = 100$, for various gap values. (a) Drag coefficient C_d. (b) Lift coefficient C_l.

c_y, (c): fairing rotation angle θ. Here, the solid lines denote results for $C_f = 0.0$, while the dashed lines represent the case $C_f = 0.1$. Through FFT analysis, we find that there are two response frequencies and they are almost the same for the two different C_f. The response frequencies are close to the vortex shedding frequency of the stationary uniform fairing system at $Re = 10,000$, $f_o = 0.167$, and the natural frequency of the cylinder, around $f_N = 0.215$, respectively. With increasing C_f from 0.0 to 0.1, the vibration in the streamwise direction does not change noticeably, but both the cross-flow displacement of cylinder and the fairing rotation decrease.

In figure 12 we plot the VIV amplitudes versus the Reynolds number, from $Re = 100$ to $Re = 10,000$. As the Reynolds number increases, the L_2 norm of the displacement in the streamwise direction, c_x, decreases from 0.09 to 0.05, the root-mean square of the displacement in the cross-flow direction, c_y, decreases from 0.18 to 0.03, and the fairing rotation, θ, decreases from 0.12 to 0.025 rad. Both drag and lift coefficients also decrease with Re. The results illustrate that the fairing experiences lower VIV motions at higher Re. However, even at the high Reynolds number $Re = 10,000$, the drag force coefficient of the fairing part is still around $C_d = 0.9$, which is much larger than the values $C_d = 0.52$ for $Re = 10^6$ for a *static* fairing in Pontaza & Menon (2008) and $C_d = 0.5 \sim 0.55$ at $Re = 1.79 \times 10^6 \sim 5.65 \times 10^6$ from experimental data in Corson *et al.* (2014).

5. Effect of gap on two different fairing-cylinder systems

In this section, we investigate the effect of the spanwise gap in the Reynolds number range from $Re = 100 \sim 1,000$. We study two different configurations: (1) the type A system, and (2) the type AB system.

5.1. *Type A system at* $Re = 100$

First we simulate the flow around a type A system at three different gap values, $G = 0.2D,\ 0.5D,\ 1.5D$. Compared to the homogeneous fairing system, a gap lowers the drag coefficient of the fairing but increases the drag coefficient of the cylinder, due to the exposure of the surface at the gap region, see figure 13. In terms of the lift coefficient, a similar trend is observed for the cylinder. However, for the fairing, only when the gap is $G = 0.5D$ the lift force is smaller than that of the homogeneous fairing-cylinder system (which is the lowest one). Moreover, figure 14 presents the time history of the lift force

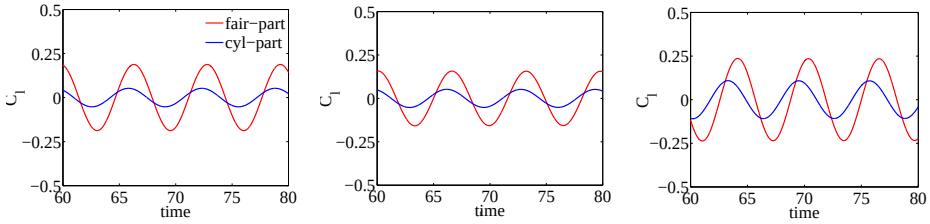

(a) (b) (c)

Figure 14: Time history of the lift coefficient of the fairing and the cylinder of a stationary type A system at $Re = 100$ for three different gap values: (a) $G = 0.2D$. (b) $G = 0.5D$. (c) $G = 1.5D$.

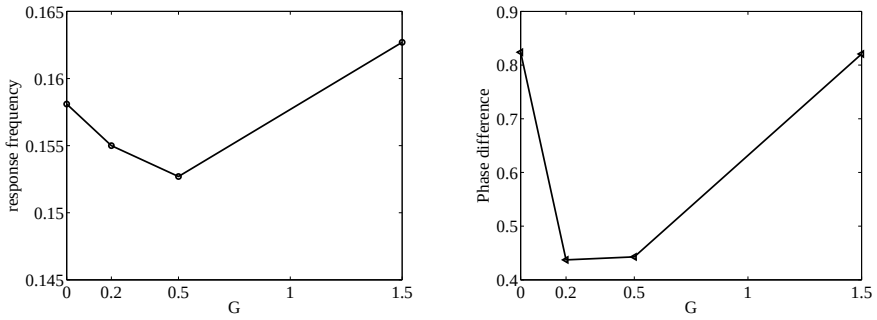

(a) (b)

Figure 15: FFT analysis of figure 14 at $Re = 100$. (a) Frequency of lift coefficient as a function of the gap. (b) Phase difference in the lift forces of the fairing and the cylinder (stationary case).

coefficients for the fairing and cylinder for different gap sizes. Through FFT analysis, the response frequency of the lift coefficients is found to be the same for the cylinder and the fairing, although there is a phase difference between the two coefficients. Figure 15 presents the response frequency and phase difference versus the gap distance. For $G = 0.2D$ or $0.5D$, the response frequency is smaller than that of the homogeneous fairing-cylinder system while for $G = 1.5D$ the response frequency is even larger than that for homogeneous fairing-cylinder system. We also note that the trend of the phase angle between the lift coefficient of the fairing and the cylinder is the same.

Next we consider the pressure distribution on the structure surface. Figure 16 shows instantaneous distributions of the pressure coefficient on the fairing surface at the $z = -0.25$ plane, where the solid symbols represent the upper surface of the fairing while the empty symbols correspond to the lower surface of the fairing. The pressure coefficient here is defined with respect to the pressure at an upstream point $(-5, 0, -0.25)$ as:

$$C_p(x, y) = \frac{2(p(x, y, -0.25) - p(-5, 0, -0.25))}{\rho_f U^2}.$$

We can see that for $G = 0.5D$, the pressure difference between the upper and lower surfaces is the smallest; this is consistent with the lowest lift force at this gap size.

The gap causes the flow to become three-dimensional even at the sub-critical Reynolds number of $Re = 100$. Figures 17(a)(c)(e) show the spanwise velocity contours at the

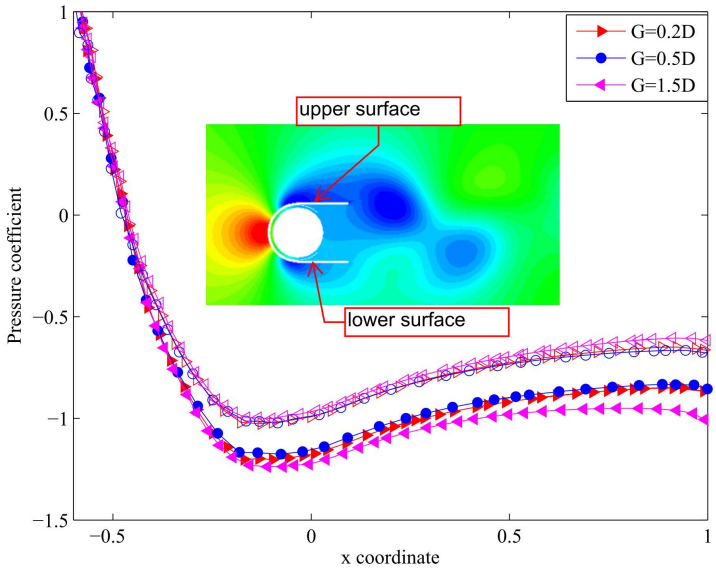

Figure 16: Distribution of the pressure coefficient on the fairing surface of a stationary type A system for $Re = 100$, at maximum lift force. Solid symbols denote the upper surface, while empty symbols denote the lower surface.

centerline plane for three gap sizes. There is a strong flow interaction between the adjacent fairings in the gap region. In the plots, the arrows denote the direction of the flow near the gap and in the wake. When the gap is small, e.g. $G = 0.2D,\ 0.5D$, the flow converges at the front of the fairing in the gap region, but in the wake the flow diverges towards the opposite spanwise directions. However, when the gap is $G = 1.5D$, the flow converges in the wake region as well. Figures 17(b),(d),(f) show iso-surfaces of streamwise vorticity (red and blue) and spanwise vorticity (yellow) around the type A system. At the upstream part of the fairing we can observe the increase of spanwise vorticity, whose intensity becomes stronger for larger gaps. In the wake of the fairing, the vorticity shows patterns resembling the mode-A instability in plain cylinder flow for $Re = 220$, with a spanwise wavelength equal to the length of the type A system. For larger gaps, the intensity of streamwise vorticity becomes stronger as well. In the far wake, the pattern of the spanwise vorticity for $G = 1.5D$ has a horseshoe form, with the direction of the horseshoe facing downstream for $G = 1.5D$, and upstream for $G = 0.2D/0.5D$.

In the previous section 4.1, we found that the free motion of the fairing decreases with increasing values of C_f. Here we adopt a frictional coefficient of $C_f = 0.2$ to simulate the free vibration and rotation of the type A system and compare with the response of the homogeneous fairing system at the same C_f and Re. For free motion, the response of the type A system is shown in figure 18. The gap causes the cylinder motion and fairing rotation to decrease. For the cross-flow cylinder displacement, the response varies in the range $0.5D \leqslant G \leqslant 1.5D$, with the smallest value at $G = 0.5D$. The force coefficient for the fairing and the cylinder are also shown in figure 19; for the drag coefficient, the trend is similar to that in the stationary configuration, i.e. C_d increases with G for the cylinder and decreases for the fairing. In contrast, the lift coefficients and angular momentum of

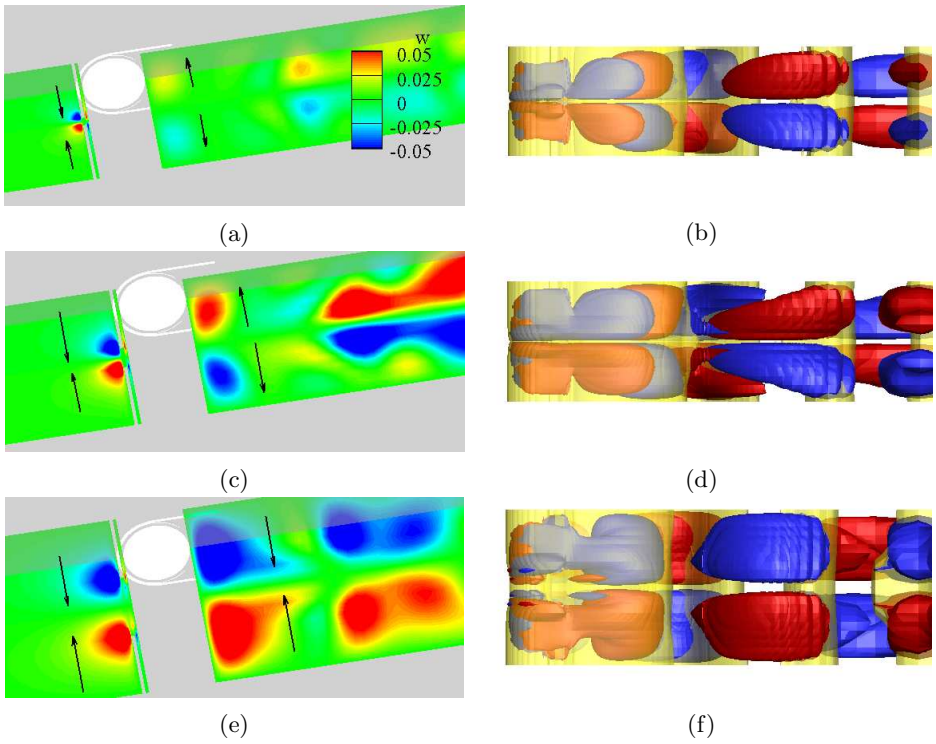

Figure 17: Three-dimensional flow patterns around the stationary type A system at $Re = 100$ for three different gaps. (a,b) $G = 0.2D$. (c,d) $G = 0.5D$. (e,f) $G = 1.5D$. Left column: spanwise velocity at the centerline-plane. Right column: vorticity iso-surfaces. $red : \omega_x = 0.1, blue : \omega_x = -0.1, yellow : \omega_z = \pm 0.5$. The arrows indicate the direction of flow near the gap and in the wake. (Plots show results at maximum lift force).

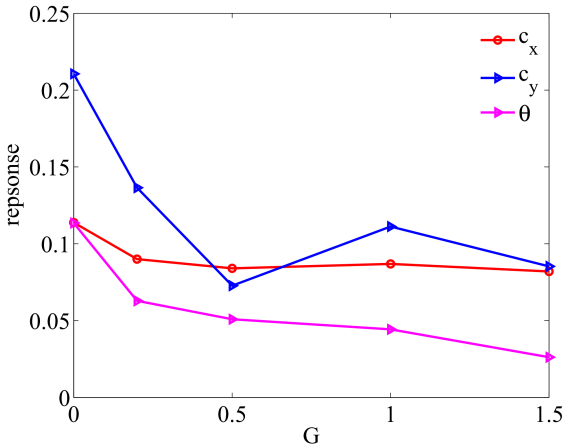

Figure 18: Effect of gap on the L_2 norm of the motion of the stationary type A system at $Re = 100$ for free vibrations. c_x and c_y denote the cylinder displacements, and θ the fairing rotation.

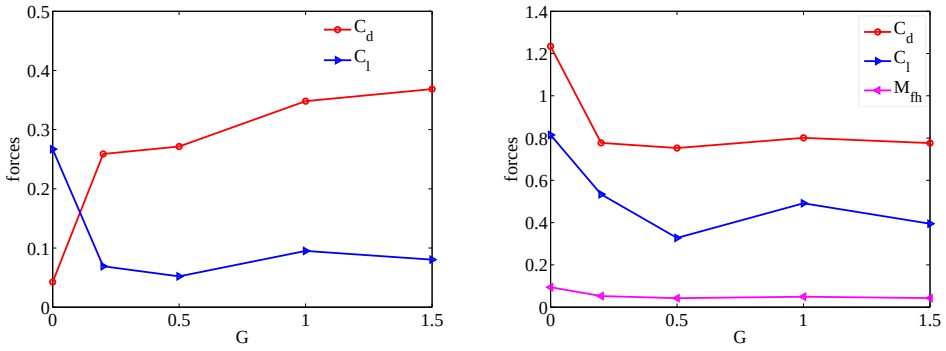

Figure 19: Effect of gap on the L_2 norm force coefficients on the type A system at $Re = 100$ for free vibrations. (a) Cylinder part. (b) Fairing part.

the fairing are smaller at larger gaps. Specifically, due to the smallest cross-flow vibration, the fairing experiences the lowest lift coefficient for a gap $G = 0.5D$.

In summary, the presence of the gap between adjacent fairings can help suppress VIV and also reduce the drag force even at low $Re = 100$, with the gap distance $G = 0.5D$ being the most effective choice from all the cases we investigated.

5.2. *Effect of Reynolds number on fairing-cylinder system of type A*

The study so far has been conducted at low Re to avoid lengthy simulations, but we will investigate next the effect of the gap at two higher Reynolds numbers, $Re = 500$ and $1,000$ at the specific gap value of $G = 0.5D$. First, we compare the results with the homogeneous fairing system and the plain cylinder, shown in figure 20 for the stationary cases. With increasing Re, the drag coefficient C_d decreases. The fairing geometry, however, can help reduce the drag force coefficient. The homogeneous fairing system reduces by 15% the drag coefficient C_d, compared to the plain cylinder case, and the fairing with gap ($G = 0.5D$) can substantially reduce further, by almost 50%, the C_d at higher Re. This is due to the faster pressure recovery in the open region in the wake between the parallel plates of the fairing, see figure 21. By comparing z-slices at $z = 0.75$, we can see that vortices are shed much farther from the tip of the fairing at $Re = 500$ and $Re = 1,000$, at a position of about $L = 3D$ and $L = 4D$ away from the cylinder center, respectively. The flow in the wake is no longer symmetric along the spanwise direction at high Re, as seen in figure 21(c)(e); in fact, the wake becomes incoherent, as shown in figure 21(d)(f).

We further investigate the VIV when free motion is allowed for a gap $G = 0.5$ and frictional coefficient $C_f = 0.2$, and compare the resulting motions with those at lower $Re = 100$ (see figure 22). These results confirm that the gap geometry suppresses VIV at high Re, but even more effectively than at lower Re. As the Reynolds number increases, the difference in the streamwise vibration of the homogeneous and type A configurations decreases as function of the gap. In contrast, the cross-flow vibration of the type A system drops quickly; e.g., at $Re = 500$ the value decreases to $c_y = 0.01$. The rotation of the fairing also decreases for the type A system at $Re = 100,\ 500$. In terms of the force coefficients, as compared to the homogeneous fairing, the gap in the type A system lowers the drag and lift force coefficients substantially, especially at higher Re. The gap distance $G = 0.5D$ at $Re = 500$ is a threshold value, beyond which VIV are totally eliminated. A typical time history of the motions of the type A system with gap $G = 0.5D$ is presented

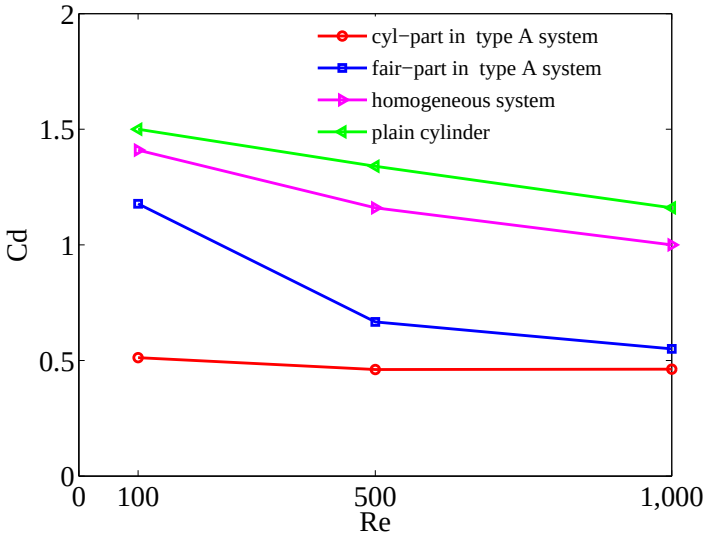

Figure 20: Variation of the mean drag coefficient C_d of the stationary configuration as function of the Reynolds number, for three different systems: plain cylinder, homogeneous fairing, and type A system.

in figure 23. For time $t > 300$, the vibration in the streamwise direction is approaching a stable value around $c_x = 0.05$, and the vibration in the cross-flow direction is in the range $-0.0015 < c_y < 0.0015$. We also observe that the time trace of the fairing rotation takes negative values, suggesting a symmetry-breaking bifurcation for some cases.

Figure 24 shows the flow structure in the wake by presenting iso-surfaces of streamwise vorticity ($\omega_x = \pm 0.25$) and spanwise vorticity ($\omega_z = \pm 0.55$), and comparing them with the results of the homogeneous fairing system for the same conditions. For the homogeneous fairing, streamwise vorticity is very well organized and the flow patterns are very similar to the flow past circular cylinders. For the type A system, the wake is widened in the gap region and the vortex street formation is delayed to a downstream position around $L = 3D$. Moreover, the vortex street is eliminated in the far wake, compared to the homogeneous fairing system.

The streamwise vorticity contours at different z-slices for these two cases are shown in figure 25 and figure 26. We find that strong streamwise vorticity only exists between the parallel plates in the wake of the homogeneous fairing system. However, for a gap between fairings, vorticity is also generated in the front side of the fairing in the gap region, resulting in two anti-symmetric vortex pairs, 'C1' and 'C2' in figure 26. The strength of the 'C1' and 'C2' pair decreases, going from the gap center towards the ends in the span-wise direction. We can see that there are two more vortex pairs, 'F1' and 'F2', generated around the fairing, and their strongest part is at about $z = \pm 1.25$. These vortex pairs interact with the vortex forming between the parallel plates in the wake, hence causing the previously coherent spanwise vorticity patterns, that feed and sustain the vortex street, to disorganize. This incoherent wake flow is the reason for the total elimination of the cylinder vibration and fairing rotation of the type A system.

Next, we investigated the VIV of the type A system for $Re = 500$ at three different reduced velocity values, $U^* = 3.5, 4.5, 6$, and compared the trajectory of motion with that of the plain cylinder and the homogeneous fairing system at the same Re. From figure 27,

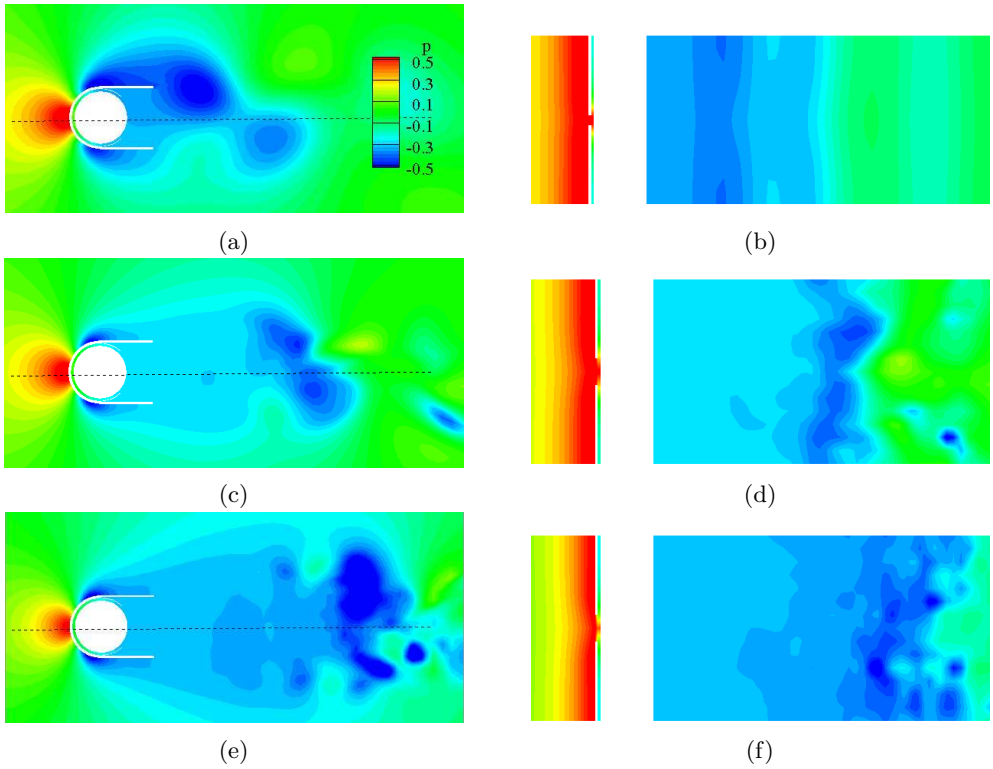

Figure 21: Pressure coefficient contours at different spanwise and cross-flow planes for the type A system with gap $G = 0.5D$ at different Re. (a) $Re = 100$ at $z = 0.75$. (b) $Re = 100$ at $y = 0$. (c) $Re = 500$ at $z = 0.75$. (d) $Re = 500$ at $y = 0$. (e) $Re = 1,000$ at $z = 0.75$. (f) $Re = 1,000$ at $y = 0$. The dashed line in the left plot denotes the planar cut presented in the plot on the right.

we can see that the homogeneous fairing system can reduce the vibration in the cross-flow direction by 80%, while the type A system with gap $G = 0.5D$ essentially eliminates the vibration, since the amplitude is smaller than $0.2\%D$. At different reduced velocities, we find that the mean streamwise vibration amplitude is around $0.05D$ for $U^* = 4.5$ and increases slightly with reduced velocity. In addition, for $U^* = 3.5, 4.65, 6$, the oscillation frequencies for c_x are $0.25, 0.2, 0.167$ separately, while the oscillation frequencies for c_y have the same value 0.2. Also, for all fairings with a gap, the mean rotation of the fairing around the cylinder is slightly negative, around 0.5 degrees.

5.3. *Fairing-cylinder system of type AB*

In the previous sections, 5.1 and 5.2, we investigated the simplified type A system. Typically, in industrial applications several fairing segments of length 3-5 diameters are fitted on each riser section. We represent this herein with the simplified type AB fairing system with periodic boundary conditions at both ends, as shown in figure 2(c), to investigate the interaction of three adjacent fairings. Due to the periodicity conditions, the two end fairings constitute effectively parts of the same fairing, while we introduce a second (middle) fairing; C_f and C_g will represent the frictional coefficients for the two fairings, respectively. The equations of motion for the type AB system have been presented in section 3.2. In the following, we consider three cases with different C_f and C_g

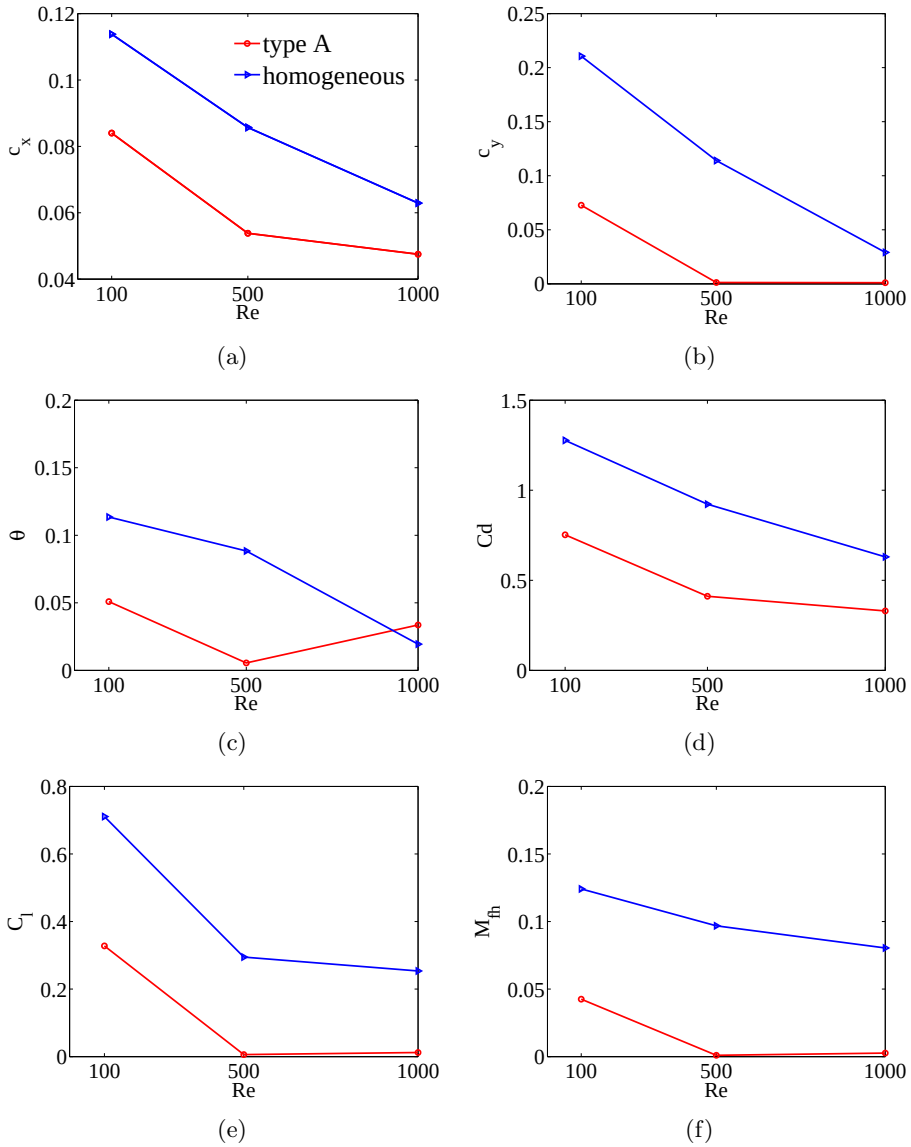

Figure 22: Comparison of the L_2 norm of the motions of the structure and the related force coefficient for the homogeneous fairing system, and for the type A system with gap $G = 0.5D$ at different Re. (a) Streamwise cylinder vibration. (b) Cross-flow cylinder vibration. (c) Rotation of fairing around the cylinder. (d) Drag coefficient for the fairing part. (e) Lift coefficient for the fairing. (f) Angular momentum of the fairing.

pairs: (a): $C_f = C_g = 0.2$, (b): $C_f = 0.2$, $C_g = 0.25$, (c): $C_f = C_g = 0.25$. Additionally, we assume that the gap between fairings is $G = 0.2D$; two Reynolds numbers, $Re = 100$ and 500, are considered.

To assess the effect of the friction, we first obtain a converged flow for a moving type AB fairing using $C_f = C_g = 0.2$. Next, we change the frictional coefficients to the values used in these three cases, and continue the simulations. Figure 28 presents time traces of

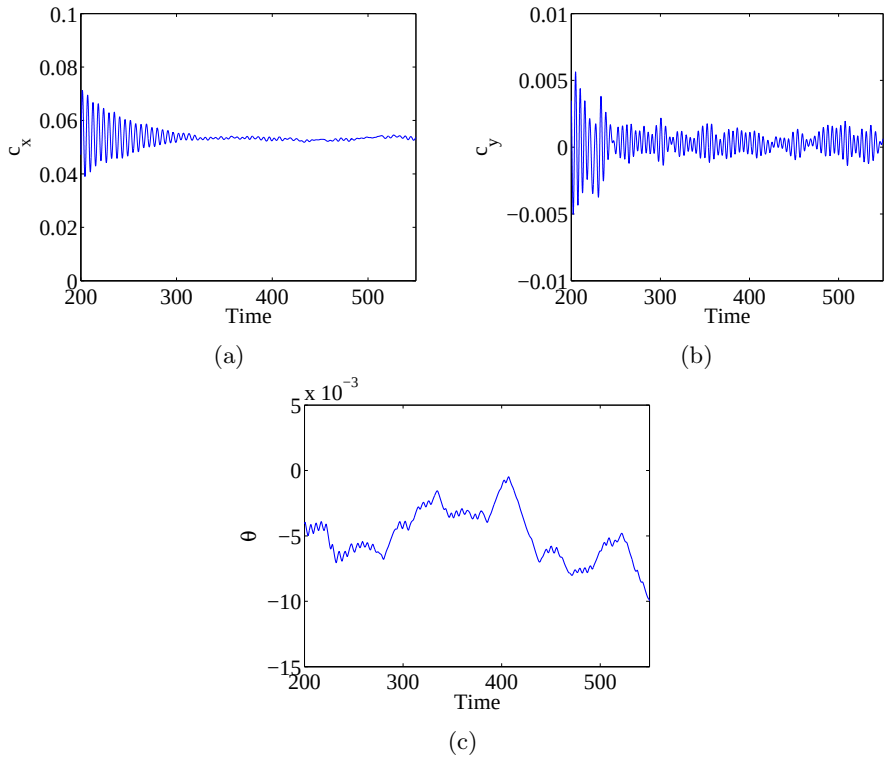

Figure 23: Time history of the motions of the type A system with gap $G = 0.5D$ at Reynolds number $Re = 500$. (a) Streamwise displacement of the cylinder c_x. (b) Cross-flow displacement of the cylinder c_y. (c) Rotational angle θ of the fairing.

the rotational angle of both fairings around the cylinder for the three different frictional coefficient pairs. The red lines are for the first fairing (A), and the blue lines are for second fairing (B) in figure 2(c). The black dotted lines denote the rotational amplitude of a homogeneous geometry at the same Reynolds number, $Re = 100$, and frictional coefficient $C_f = 0.2$ for the first case; and $C_f = 0.25$ for the third case. For the same frictional coefficients, the rotational response of a type AB fairing is very similar to type A, with the two fairings rotating almost at the same rate, see figure 28(a)(c). However, for different frictional coefficients, $C_f = 0.2$, $C_g = 0.25$, the time traces of rotation for the two fairings, A and B, are totally different. The difference is increasing with time and the mean rotational angle deviates from the zero position, suggesting a symmetry-breaking bifurcation.

The difference in rotational response of the two fairings triggers different flow patterns behind each fairing of the type AB system. Figure 29 presents vorticity and velocity contours for three cases. The left column shows iso-surfaces of spanwise vorticity ($\omega_z = \pm 0.5$) in grey and iso-surfaces of streamwise vorticity ($\omega_z = \pm 0.3$) colored by pressure contour level. The right column shows the spanwise velocity at the centerline in the y-plane, with the arrows denoting the spanwise flow direction. Moreover, Figure 30 shows z-slices of streamwise vorticty at the positions $z = -2.7, -2.2, -1.6 - 1.0, -0.5$ (black horizontal lines in Figure 29(a)). When the same frictional coefficient is used for both fairings, the flow structure is similar for each fairing (see top and bottom rows of figure 29 and figure 30(a)(c)). The streamwise vorticty in the wake of fairing B ($z = -2.7, 2.2$)

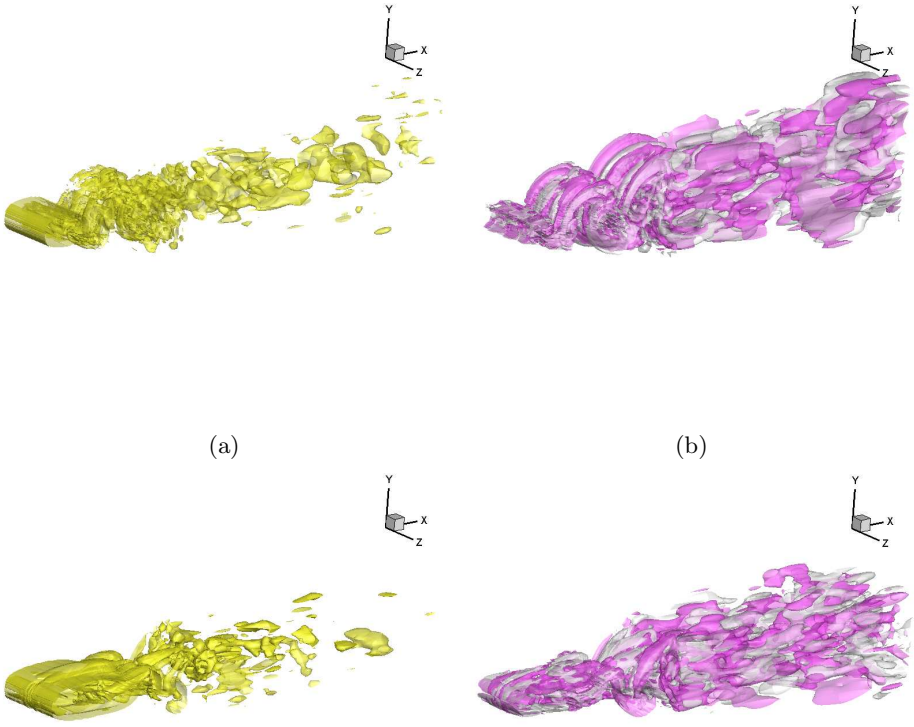

(a) (b)

(c) (d)

Figure 24: Iso-surfaces of spanwise vorticity (in yellow) ($\omega_z = \pm 0.55$) and streamwise vorticity (in purple and gray) ($\omega_x = \pm 0.25$) for (a,b) moving homogeneous fairing-cylinder system; (c,d) moving type A system with gap $G = 0.5D$; for frictional coefficient $C_f = 0.2$ and Reynolds number $Re = 500$.

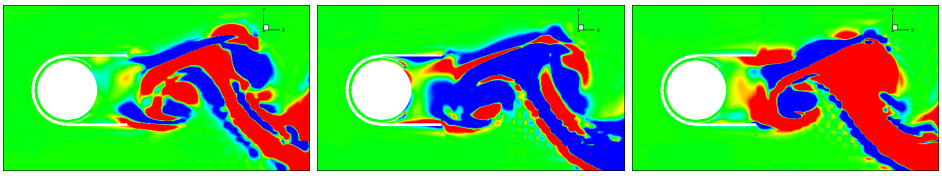

(a) (b) (c)

Figure 25: Streamwise vorticity ($-0.25 \leqslant \omega_x \leqslant 0.25$) contours at different z-slices, for a moving homogeneous fairing system at frictional coefficient $C_f = 0.2$ and Reynolds number $Re = 500$. (a) $z = -0.5$. (b) $z = 0$. (c) $z = 0.5$.

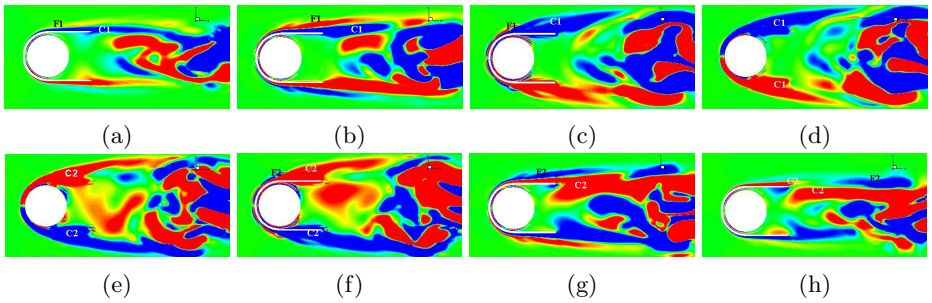

Figure 26: Streamwise vorticity ($-0.25 \leqslant \omega_x \leqslant 0.25$) contours at different z-slices for a moving type A system with gap $G = 0.5D$ at frictional coefficient $C_f = 0.2$ and Reynolds number $Re = 500$. (a) $z = -1.75$. (b) $z = -1.25$. (c) $z = -0.3$. (d) $z = -0.25$. (e) $z = 0.25$. (f) $z = 0.3$. (g) $z = 1.25$. (h) $z = -1.75$.

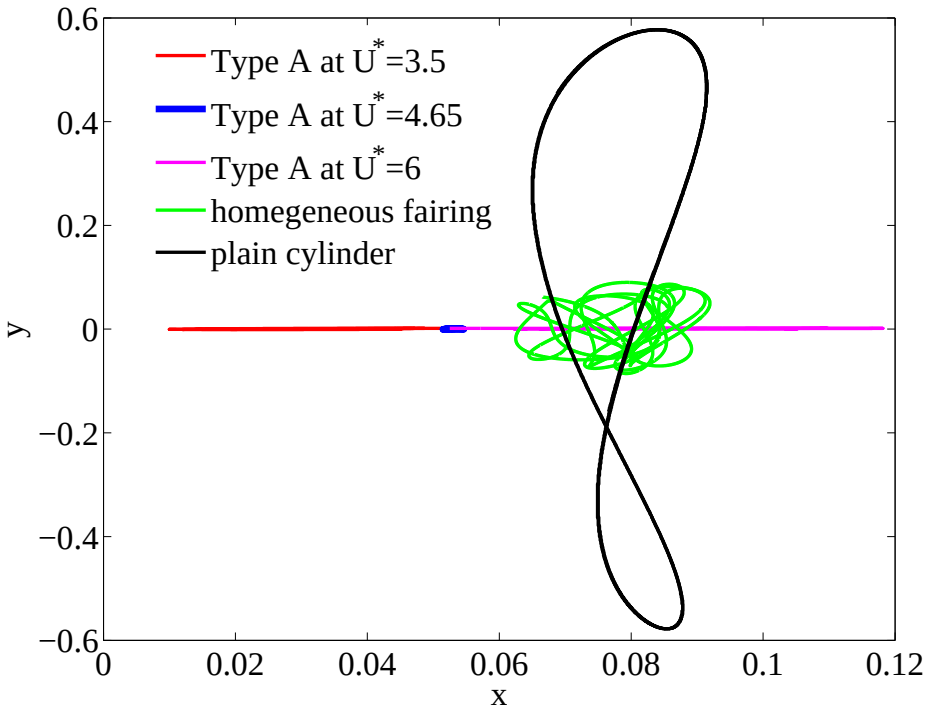

Figure 27: Trajectories of motion for the fairing-cylinder system at Re = 500. The black line corresponds to a plain cylinder, the green line to a homogeneous fairing-cylinder system, and the red, blue and purple lines are for the fairing-cylinder system of type A with gap $G = 0.5D$ at different values of the reduced velocity.

has the same pattern as the wake of fairing A ($z = -1.0, -0.5$). In the gap region, there is either no or very small streamwise vorticity depending on the frictional coefficient. However, when different frictional coefficients are used, $C_f = 0.2$, $C_g = 0.25$, the flow is changed, as shown in figure 29 (middle plots) and figure 30(b). Because of the larger rotational amplitude for fairing A, the streamwise vorticity in the wake of fairing A is

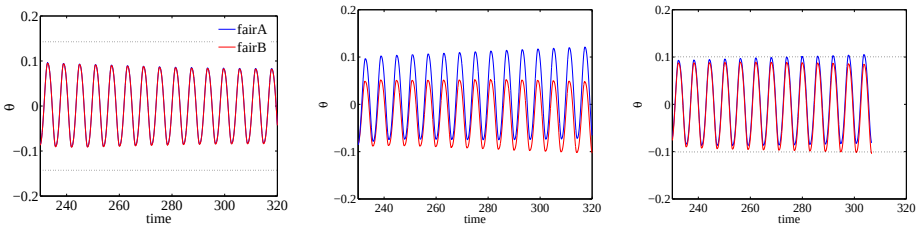

(a) (b) (c)

Figure 28: Time history of the rotation angles of the AB fairings. Red lines: first fairing; blue lines: second fairing; at $Re = 100$. (a) $C_f = C_g = 0.2$. (b) $C_f = 0.2,\ C_g = 0.25$. (c) $C_f = C_g = 0.25$. The dotted lines are for a homogeneous fairing-cylinder system for the same parameters.

much stronger than for fairing B. There is also significant streamwise vorticity in the gap region; see z-slice contour at $z = -1.6$ in the middle plot in figure 30(b). Unlike the flow for the type A fairing (Figure 17), the flow separates in the gap region at the front (upstream) end of each fairing for the type AB system. Also the wake exhibits different patterns for the three cases, uniform, versus A and AB. When the frictional coefficient is the same across the span, i.e. for the first and third cases, the flow is converging in the gap region. With different frictional coefficients, $C_f = 0.2,\ C_g = 0.25$, the flow wake exhibits a high degree of interaction in the gap region, with the fluid gathering from fairing B to fairing A, or vice-versa. The interaction is stronger in the wake around $L = 2D$ (shown though a black circle).

Next, we increase the Reynolds number to $Re = 500$ for the type AB fairing and investigate the effect of the frictional coefficients. Figure 31 shows the time history of the rotational angle for each fairing. There is significant difference in the response for time $t < 300s$; beyond this range, both responses converge, approaching the same small negative value at around $t > 375s$ of about -0.5 deg. We can conclude that the effect of the frictional coefficient of the fairings is negligible at higher Reynolds numbers. If we further investigate z-slices of streamwise vorticity at various positions along the span, as shown in figure 32, the flow is much different than for the homogeneous fairing, as the development of organized spanwise vortices is significantly delayed, to about three of four diameters downstream. There are some similarities of the flow patterns with the type A system, but also major differences (see Figure 25), as the wake is narrower and flow separation at the fairing is significantly reduced.

6. Conclusion

The principal result of the present study is that for specific values of the gap between adjacent segments of U-shaped fairings attached on a cylinder in cross-flow, vortex induced vibrations of the cylinder are suppressed, both in-line and cross-flow, and fairing rotations are also reduced to small values, resulting also in reduction of the drag coefficient by about 50%. The effects of the gap increase with Reynolds number, by generating strong three-dimensionality in the flow, which disrupts the formation of coherent spanwise vortices until three of four diameters downstream in the wake.

We considered three different fairing geometries (figure 2), a homogeneous one, without gap; a single gap with two adjacent fairings; and two gaps separating three adjacent fairings; with periodicity conditions applied at the ends for all cases. The gap was changed

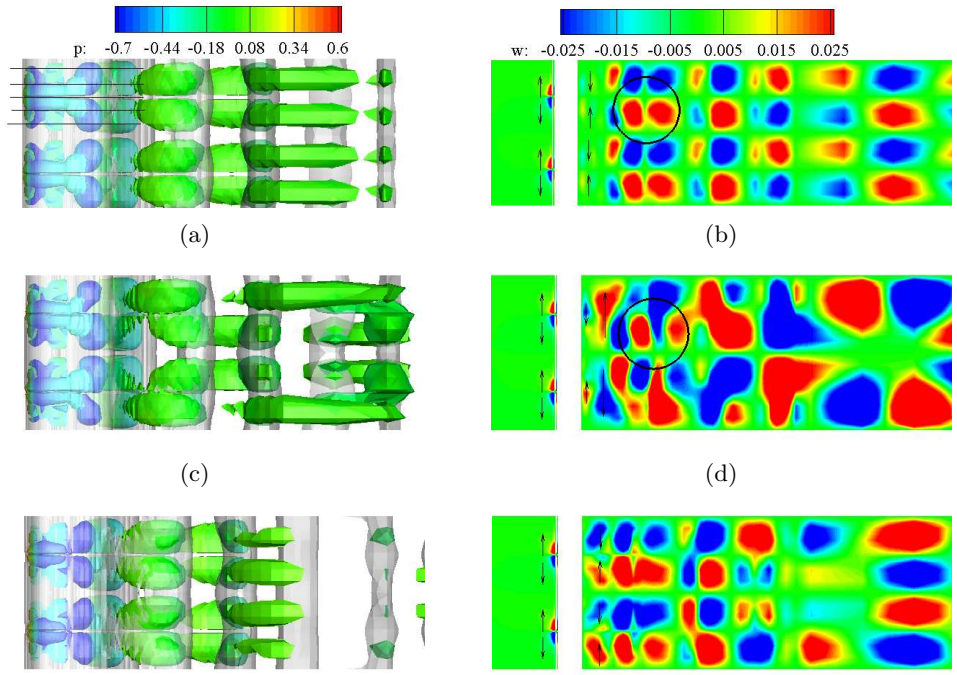

Figure 29: Flow structure for the type AB fairing at $Re = 100$ in terms of: (a,c,e) iso-surfaces of spanwise vorticity ($\omega_z = \pm 0.5$) colored in grey, and iso-surfaces of streamwise vorticity ($\omega_x = \pm 0.3$) colored by pressure contour level; and (b,d,f) spanwise velocity shown at the centerline y-plane for type AB fairing at $Re = 100$ with gap $G = 0.2D$. (a,b) $C_f = C_g = 0.2$. (c,d) $C_f = 0.2,\ C_g = 0.25$. (e,f) $C_f = C_g = 0.25$.

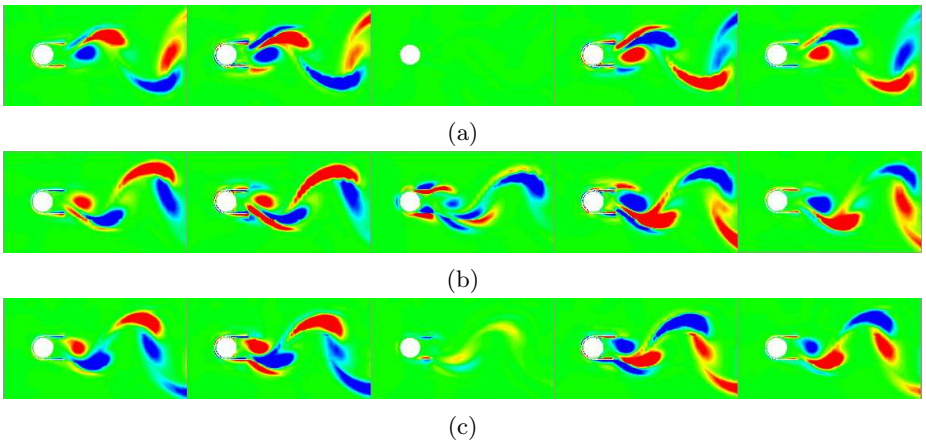

Figure 30: For AB fairings, streamwise vorticity contours ($-0.25 \leqslant \omega_x \leqslant 0.25$) at different z-slices at $z = -2.7, -2.2, -1.6 - 1.0, -0.5$ (black horizontal lines in 29(a)), at $Re = 100$ with gap $G = 0.2D$. (a) $C_f = C_g = 0.2$. (b) $C_f = 0.2,\ C_g = 0.25$. (c) $C_f = C_g = 0.25$.

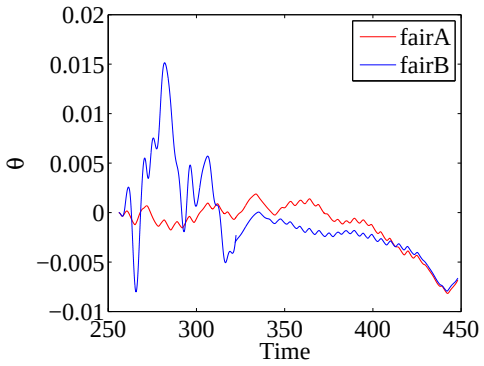

Figure 31: Time history of the rotation angle in radians for each fairing of an AB system for different frictional coefficients: $C_f = 0.2,\ C_g = 0.25$ at $Re = 500$ with gap $G = 0.2D$.

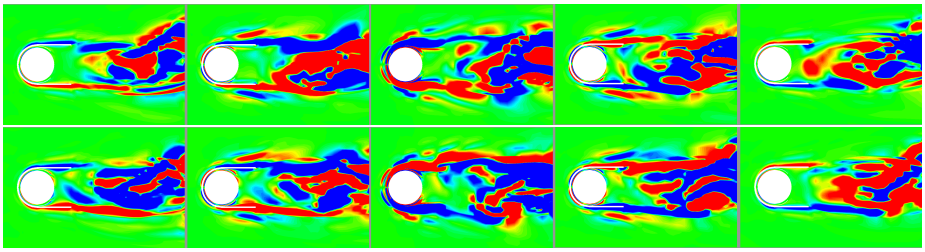

Figure 32: Streamwise vorticity contours ($-0.25 \leqslant \omega_x \leqslant 0.25$) at different z-slices of the type AB fairing system, at $z = -2.7, -2.2, -1.7 - 1.0, -0.5$ in the first row and at $z = 0.5, 1.0, 1.7, 2.2, 2.7$ in the second row, at $Re = 500$ for $C_f = 0.2,\ C_g = 0.25$ and with gap $G = 0.2D$.

from 0.2D up to 1.5 D, and the Reynolds number from 100 to 10,000. We investigated the effect of the gap on the fluid forces and the translational and rotational motions of each system. While compared to a plain cylinder a homogeneous fairing system reduces drag by 15%, a type A gap system can reduce the drag force coefficient by about 50%. For a homogeneous fairing, the cross-flow amplitude is reduced by about 80%, but for fairings with gaps longer than $0.5D$, vibrations are almost completely eliminated.

As shown in figures 25, 26 and 32, while a uniform fairing delays the formation of spanwise vortical patterns by a length roughly equal to its streamwise length, a segmented fairing with gaps further delays coherent spanwise vortices by another two diameters to four diameters, resulting in much smaller unsteady forces and hence negligible vibration.

The effect of friction in the fairing rotation was found in previous studies to be important, but we found relatively small effect from friction, even when adjacent segments have different frictional coefficients; in the latter case, however, symmetry may be broken, resulting in slightly rotated positions of adjacent fairings relative to each other, also affecting the flow symmetry.

Acknowledgments

The authors gratefully acknowledge support by the Chevron-MIT University Partnership Program. FFX also wishes to thank Dr. Xiaoning Zheng and Dr. Hessam Babaee of the MIT Sea Grant Program for their thoughtful disscussions of this paper.

REFERENCES

Allen, D. W., Henning, D. L., Haws, J. H., McMillan, D. W. & McDaniel, R. B. 2003 Partial helical strake for vortex-induced-vibrationsuppression. US Patent 6,561,734.

Allen, D. W., Lee, L. & Henning, D. L. 2008 Fairings versus helical strakes for suppression of vortex induced vibration: Technical comparisons. In *Proceedings of the Offshore Technology Conference*.

Assi, G. R. S., Bearman, P. W. & Kitney, N. 2009 Low drag solutions for suppressing vortex-induced vibration of circular cylinders. *Journal of Fluids and Structures* **25** (4), 666–675.

Baek, H. & Karniadakis, G. E. 2009 Suppressing vortex-induced vibrations via passive means. *Journal of Fluids and Structures* **25** (5), 848–866.

Baek, H. & Karniadakis, G. E. 2011 Sub-iteration leads to accuracy and stability enhancements of semi-implicit schemes for the Navier-Stokes equations. *Journal of Computational Physics* **230** (12), 4384 – 4402.

Baek, H. & Karniadakis, G. E. 2012 A convergence study of a new partitioned fluid–structure interaction algorithm based on fictitious mass and damping. *Journal of Computational Physics* **231** (2), 629–652.

Bao, Y. & Tao, J. 2013 The passive control of wake flow behind a circular cylinder by parallel dual plates. *Journal of Fluids and Structures* **37**, 201–219.

Bearman, P. W. 1965 Investigation of the flow behind a two-dimensional model with a blunt trailing edge and fitted with splitter plates. *Journal of Fluid Mechanics* **21** (02), 241–255.

Bearman, P. W. & Branković, M. 2004 Experimental studies of passive control of vortex-induced vibration. *European Journal of Mechanics-B/Fluids* **23** (1), 9–15.

Causin, P., Gerbeau, J. F. & Nobile, F. 2005 Added-mass effect in the design of partitioned algorithms for fluid–structure problems. *Computer Methods in Applied Mechanics and Engineering* **194** (42), 4506–4527.

Chen, W., Xin, D., Xu, F., Li, H., Ou, J. & Hu, H. 2013 Suppression of vortex-induced vibration of a circular cylinder using suction-based flow control. *Journal of Fluids and Structures* **42**, 25–39.

Corson, D., Cosgrove, S. & Constantinides, Y. 2014 Application of CFD to predict the hydrodynamic performance of offshore fairing designs. In *ASME 2014 33rd International Conference on Ocean, Offshore and Arctic Engineering*, pp. V002T08A079–V002T08A079. American Society of Mechanical Engineers.

Dong, S., Triantafyllou, G. S. & Karniadakis, G. E. 2008 Elimination of vortex streets in bluff-body flows. *Physical review letters* **100** (20), 204501.

Every, M. J., King, R. & Weaver, D. S. 1982 Vortex-excited vibrations of cylinders and cables and their suppression. *Ocean Engineering* **9** (2), 135–157.

Galvao, R., Lee, E., Farrell, D., Hover, F., Triantafyllou, M., Kitney, N. & Beynet, P. 2008 Flow control in flow–structure interaction. *Journal of Fluids and Structures* **24** (8), 1216–1226.

Gu, F., Wang, J. S., Qiao, X. Q. & Huang, Z. 2012 Pressure distribution, fluctuating forces and vortex shedding behavior of circular cylinder with rotatable splitter plates. *Journal of fluids and structures* **28**, 263–278.

Hughes, T. J. R., Liu, W. K. & Zimmermann, T. K. 1981 Lagrangian-Eulerian finite element formulation for incompressible viscous flows. *Computer Methods in Applied Mechanics and Engineering* **29** (3), 329 – 349.

Karniadakis, G. E. & Sherwin, S. 2013 *Spectral/hp element methods for computational fluid dynamics*. Oxford University Press.

Korkischko, I. & Meneghini, J. R. 2012 Suppression of vortex-induced vibration using moving surface boundary-layer control. *Journal of Fluids and Structures* **34**, 259–270.

Kwon, K. & Choi, H. 1996 Control of laminar vortex shedding behind a circular cylinder using splitter plates. *Physics of Fluids (1994-present)* **8** (2), 479–486.

Luo, X., Epps, B., Chryssostomidis, C. & Karniadakis, G. E. 2011 Comparison of turbulence models for simulating flow in waterjets. In *Proceedings of the 11th International Conference on Fast Sea Transportation*. American Society of Naval Engineers.

Owen, J. C., Bearman, P. W. & Szewczyk, A. A. 2001 Passive control of VIV with drag reduction. *Journal of Fluids and Structures* **15** (3), 597–605.

Pontaza, J. P., Kotikanyadanam, M., Moeleker, P., Menon, R. G. & Bhat, S. 2012 Fairing evaluation based on numerical simulation. In *ASME 2012 31st International Conference on Ocean, Offshore and Arctic Engineering*, pp. 897–905. American Society of Mechanical Engineers.

Pontaza, J. P. & Menon, R. G. 2008 Numerical simulations of flow past an aspirated fairing with three degree-of-freedom motion. In *ASME 2008 27th International Conference on Offshore Mechanics and Arctic Engineering*, pp. 799–807. American Society of Mechanical Engineers.

Pontaza, J. P., Menon, R. G. & Chen, H. C. 2007 Three-dimensional numerical simulations of flows past smooth and rough/bare and helically straked circular cylinders allowed to undergo two degree-of-freedom motions. In *ASME 2007 26th International Conference on Offshore Mechanics and Arctic Engineering*, pp. 921–930. American Society of Mechanical Engineers.

Serson, D., Meneghini, J. R., Carmo, B. S., Volpe, E. V. & Gioria, R. S. 2014 Wake transition in the flow around a circular cylinder with a splitter plate. *Journal of Fluid Mechanics* **755**, 582–602.

Trim, A. D., Braaten, H., Lie, H. & Tognarelli, M. A. 2005 Experimental investigation of vortex-induced vibration of long marine risers. *Journal of fluids and structures* **21** (3), 335–361.

Williamson, C. H. K. & Govardhan, R. 2004 Vortex-induced vibrations. *Annu. Rev. Fluid Mech.* **36**, 413–455.

Williamson, C. H. K. & Govardhan, R. 2008 A brief review of recent results in vortex-induced vibrations. *Journal of Wind Engineering and Industrial Aerodynamics* **96** (6), 713–735.

Yu, Y., Baek, H. & Karniadakis, G. E. 2013 Generalized fictitious methods for fluid–structure interactions: Analysis and simulations. *Journal of Computational Physics* **245**, 317–346.

Yu, Y., Xie, F., Yan, H., Constantinides, Y., Oakley, O. & Karniadakis, G. E. 2015 Suppression of vortex-induced vibrations by fairings: A numerical study. *Journal of Fluids and Structures* **54**, 679–700.

Zdravkovich, M. M. 1981 Review and classification of various aerodynamic and hydrodynamic means for suppressing vortex shedding. *Journal of Wind Engineering and Industrial Aerodynamics* **7** (2), 145–189.